Draft version November 22, 2024
Typeset using LaTeX default style in AASTeX631

Intrinsic and Environmental Effects on the Distribution of Star Formation in TNG100 Galaxies

Bryanne McDonough [1,2] Olivia Curtis [3,2] and Tereasa G. Brainerd [2]

[1] Department of Physics, Northeastern University, 360 Huntington Ave, Boston, MA
[2] Institute for Astrophysical Research, Boston University, 725 Commonwealth Ave, Boston, MA
[3] Department of Astronomy & Astrophysics, The Pennsylvania State University, 251 Pollock Road, University Park, PA

Submitted to ApJ

ABSTRACT

We present radial profiles of luminosity-weighted age (age$_L$) and $\Delta\Sigma_{\rm SFR}$ for various populations of high- and low- mass central and satellite galaxies in the TNG100 cosmological simulation. Using these profiles, we investigate the impact of intrinsic and environmental factors on the radial distribution of star formation. For both central galaxies and satellites, we investigate the effects of black hole mass, cumulative AGN feedback energy, morphology, halo mass, and local galaxy overdensity on the profiles. In addition, we investigate the dependence of radial profiles of the satellite galaxies as a function of the redshifts at which they joined their hosts, as well as the net change in star-forming gas mass since the satellites joined their host. We find that high-mass ($M_* > 10^{10.5} M_\odot$) central and satellite galaxies show evidence of inside-out quenching driven by AGN feedback. Effects from environmental processes only become apparent in averaged profiles at extreme halo masses and local overdensities. We find that the dominant quenching process for low-mass galaxies ($M_* < 10^{10} M_\odot$) is environmental, generally occurring at low halo mass and high local galaxy overdensity for low-mass central galaxies and at high host halo masses for low-mass satellite galaxies. Overall, we find that environmental processes generally drive quenching from the outside-in.

1. INTRODUCTION

The advent of integral field spectroscopy (IFS) surveys has revolutionized the study of star formation on resolved scales outside of the Milky Way, leading to new insights into how galaxies grow and evolve. Here, we briefly describe

Corresponding author: Bryanne McDonough
br.mcdonough@northeastern.edu

these insights as they relate to the radial distribution of properties related to star formation; we direct readers to Sánchez (2020) and Sánchez et al. (2021) for a comprehensive review. At the onset of star formation, the gas reservoir of galaxies is centrally concentrated. Over time, stars form out of molecular gas at larger and larger radii. This results in the negative gradient in the stellar mass surface density that is seen at present-day (e.g., González Delgado et al. 2014; Sánchez 2020; Pan et al. 2024). This gradient, sometimes referred to as "inside-out growth" is more extreme in more massive/early-type galaxies.

The cessation of star formation also appears to occur from the inside-out, at least for massive galaxies. This is reflected by negative gradients in the luminosity-weighted age of massive galaxies over large scales ($R/R_e \approx 0 - 3$), e.g., González Delgado et al. (2014); Zheng et al. (2017); Sánchez (2020). The central suppression of specific star formation rates (sSFR), or similar parameters, in massive galaxies ($M_*/M_\odot \gtrsim 10^{10}$) in the observed universe has been well documented in the literature (e.g., González Delgado et al. 2014; Ellison et al. 2018; Spindler et al. 2018; Bluck et al. 2020b; Sánchez 2020; Sánchez et al. 2021; Pan et al. 2024). The tight correlation between the mass of the central supermassive black hole (SMBH) and other galaxy properties, including stellar mass and star formation rate (SFR), indicates that SMBHs play a significant role in quenching massive galaxies. In the parlance of Peng et al. (2010), 'mass quenching' refers to processes inherently linked to the mass of a galaxy that act to quench star formation, leading to larger fractions of quenched galaxies with increasing stellar mass and SMBH mass (e.g., Peng et al. 2010; Bluck et al. 2020a). Bluck et al. (2020b) used a random forest machine learning algorithm to determine the importance of various parameters for predicting quenching in central galaxies observed by MaNGA (Bundy et al. 2015). They found that central velocity dispersion, which is tightly correlated with SMBH mass (e.g., Saglia et al. 2016), was the most predictive variable. A SMBH can regulate star formation via AGN energy imparted onto cool gas. The exact mechanisms by which AGN feedback results in a cessation of star formation is still an active area of research. However, it may be the result of heating or removal of gas reservoirs, or the introduction of turbulence, resulting in a decrease in the star formation efficiency (SFE). SFE has been found to decrease during the 'green valley' stage of galaxy evolution, the transition from actively star-forming to retired/quenched (e.g., Colombo et al. 2020; Villanueva et al. 2024). The cause of decreasing SFE and its role in shutting down star formation is still being explored.

Determining which parameters drive quenching in galaxies is complicated by the inter-correlation of variables, particularly those that are intrinsic to a galaxy. This may be especially true for parameters that characterize galaxy morphology. For example, Bluck et al. (2020b) found that bulge-to-total stellar mass ratio (B/T) was the fourth most important parameter for quenching in central galaxies, but they note that its importance may be overestimated due to the correlation of B/T with central velocity dispersion. In addition, Bluck et al. (2014) identified bulge mass as being tightly correlated with the quenched fraction of galaxies.

The role of morphology in shaping the radial distribution of stellar ages and local sSFR has also been investigated by González Delgado et al. (2014, 2016) in the CALIFA survey (García-Benito et al. 2015). González Delgado et al. (2014) found that the shape of the average luminosity-weighted age (age_L) profile varied as a function of stellar mass and concentration index. Martig et al. (2009) proposed that the presence of a bulge can stabilize gas against the gravitational collapse and fragmentation necessary for star formation. It is also possible that the presence of a bulge and quiescence can be the result of similar evolutionary processes; e.g., mergers. Due to the correlation of morphology with stellar mass, the role of morphology in galaxy quenching remains unclear.

The halo environment in which a galaxy resides can also affect star formation properties via processes that remove, heat, or compress gas, such as galaxy-galaxy harassment, ram pressure stripping, and dynamical stripping (see, e.g., Peng et al. 2012). Corcho-Caballero et al. (2023) found that most galaxies that quenched relatively rapidly (over ~ 1 Gyr timescales) were low-mass satellite galaxies. The random forest analysis performed by Bluck et al. (2020b) indicated that, unlike central galaxies, both intrinsic and environmental parameters are predictive of quenching in satellite galaxies. In their work, Bluck et al. (2020b) found that environmental parameters, namely local galaxy overdensity and host halo mass, were most important for predicting quenching in low-mass ($M_*/M_\odot < 10^{10}$) satellite galaxies. This boundary, $M_*/M_\odot \approx 10^{10}$, has been indicated as the threshold above which quenching can be driven by a central AGN, also known as mass quenching (Peng et al. 2010, 2012). McDonough et al. (2023) found a similar threshold at $10^{10} < M_*/M_\odot < 10^{10.5}$ for galaxies in the TNG100 simulation, with more massive galaxies showing clear evidence of inside-out mass quenching in radial profiles of age_L.

Complimentary to the progress in spatially resolving galaxies in observations, cosmological hydrodynamic simulations have improved in both scale and resolution, as well as the degree of agreement between observations and the predictions of the simulations. Key to the improvement in agreement between observations and simulations has been the implementation and improvement of feedback models in the simulations. These feedback models approximate the impact of active galactic nucelei (AGN) and supernovae, decreasing the efficiency of star formation and preventing early depletion of gas reservoirs (see, e.g., Naab & Ostriker 2017; Donnari et al. 2019). However, since the actual processes that drive AGN and supernovae feedback occur on scales that are not resolved in most simulations, these effects must be approximated, requiring assumptions regarding how and where feedback energy is imparted in simulated galaxies.

In McDonough et al. (2023), we demonstrated that TNG100, part of the IllustrisTNG cosmological magnetohydrodynamic simulation suite (Nelson et al. 2018; Pillepich et al. 2018; Springel et al. 2018; Naiman et al. 2018; Marinacci et al. 2018; Nelson et al. 2019), reproduced both the observed resolved star formation main sequence (rSFMS) and the radial distribution of star formation in main sequence, green valley, and quenched galaxies. The rSFMS, or $\Sigma_* - \Sigma_{\mathrm{SFR}}$ relation, was first presented by Sánchez et al. (2013) and Wuyts et al. (2013) and was later characterized by Cano-Díaz et al. (2016). As demonstrated by Nelson et al. (2021), the location within galaxies at which feedback energy is injected is critical for accurately reproducing the observed radial distribution of star formation. Both TNG100 and its predecessor, Illustris-1, adopted AGN feedback models with prescriptions for high- and low- accretion rate modes. Illustris-1 (Vogelsberger et al. 2014; Nelson et al. 2015) adopted an AGN feedback model that, at low accretion rates, injected feedback energy as thermal energy in large bubbles displaced from central galaxies. In contrast, the low-accretion state of the AGN feedback model in the IllustrisTNG simulations (Weinberger et al. 2017) injects kinetic energy into gas immediately surrounding the supermassive black hole at the galaxy center.

Nelson et al. (2021) computed the radial profiles of sSFR for galaxies in the 50 Mpc simulation box of IllustrisTNG (TNG50), Illustris-1, and 3D-HST observations. From this, they found that the observed central suppression of star formation in massive galaxies was reproduced in TNG50 galaxies, but not in Illustris-1 galaxies. Nelson et al. (2021) attribute this improvement to the difference in feedback models, since the TNG and Illustris-1 simulations are similar in other respects, including the same initial conditions and star formation prescriptions.

In this article, we adopt a broad but commonly used definition of 'quenching,' which we use to describe the reduction and eventual cessation of star formation in galaxies. In this parlance, 'quenched' galaxies are those that have ceased forming stars at significant levels, often defined by their position on a color-magnitude or $M_* - \mathrm{SFR}$ diagrams. We note that there is some discussion in the literature (e.g., Corcho-Caballero et al. 2023) that 'quenching' be reserved to describe rapid cessation of star formation. Corcho-Caballero et al. (2023) argues for a distinction between galaxies that quench rapidly and those that 'retire' their star formation over longer timescales. While we adopt a broad definition of quenching in this article, we acknowledge that such a distinction may be relevant to future analyses.

In this paper, we investigate the dependence of radial profiles of luminosity-weighted age and $\Delta\Sigma_{\mathrm{SFR}}$, the offset from the resolved star formation main sequence (rSFMS, or the $\Sigma_* - \Sigma_{\mathrm{SFR}}$ relation), on various intrinsic and environmental parameters. The paper is organized as follows. In § 2, we provide a brief overview of TNG100, along with a discussion of the ways in which we derive parameters from the simulation data. In § 3, we present results for radial profiles of age_L and $\Delta\Sigma_{\mathrm{SFR}}$ for galaxies as a function of various intrinsic parameters. In § 4, we explore the dependence of radial profiles of age_L and $\Delta\Sigma_{\mathrm{SFR}}$ on environmental parameters. A discussion of the implications of our results, in the context of the existing literature, is presented in § 5, and a summary of our main results and conclusions is given in § 6. In Appendix A, we present correlations that exist between the various parameters that we explored in the main body of the paper. In Appendix B, we summarize the normalization and gradients for the radial profiles presented in § 3 and § 4. In Appendix C, we explore the mass-dependence of the profile normalizations.

2. METHODOLOGY

The methodology by which we select our galaxy sample is identical to the methodology we used in McDonough et al. (2023). That is, a sample of $\sim 60,000$ luminous ($M_r < -14.5$) simulated galaxies at $z = 0$ was obtained from the $75^3 h^{-3}\mathrm{Mpc}^3$ volume TNG100-1 simulation (hereafter, TNG100). The TNG100 simulation is part of the IllustrisTNG project, a suite of publicly available ΛCDM magnetohydrodynamical simulations that adopted a Planck Collaboration (2016) cosmology with the following parameter values: $\Omega_{\Lambda,0} = 0.6911$, $\Omega_{m,0} = 0.3089$, $\Omega_{b,0} = 0.0486$, $\sigma_8 = 0.8159$, $n_s = 0.9667$, and $h = 0.6774$. We take the galaxy stellar mass to be the total mass of all stellar particles that are bound to each galaxy according to the `SubFind` catalog. From the Stellar Projected Sizes supplementary catalog (Genel et al. 2018), we obtain r-band half-light radii, which we will refer to as effective radii, R_e. We obtain magnitudes from the SDSS Photometry, Colors, and Mock Fiber Spectra catalog (Nelson et al. 2018). It is also important to note that, unlike R_e and galaxy magnitudes (which are directly comparable to observed galaxy properties), the stellar masses we adopt for TNG100 galaxies are not directly comparable to the stellar masses of observed galaxies (which are typically obtained by modelling of the spectral energy distribution).

Here, galaxy sample and data products are identical to those that we used in McDonough et al. (2023). We provide only a brief description here, and the reader is referred to Section 2 of McDonough et al. (2023) for a full description of the catalogs and galaxy sample selection criteria. We ensure sufficient resolution of the galaxies by limiting the sample to galaxies that contain at least $1,000$ stellar particles within $2R_e$ and have a physical size of $R_e > 4$ kpc. The most massive galaxy in a given friends-of-friends group is defined to be the central galaxy, and all other group members are considered to be satellites. Our full sample consists of $4,605$ central galaxies and $1,592$ satellites. From McDonough et al. (2023), we know that the shapes of the radial profiles differ significantly for high-mass and low-mass galaxies, and we define these to be $M_* > 10^{10.5} M_\odot$ and $M_* < 10^{10} M_\odot$, respectively. The division of our sample into low- and high-mass galaxies is based on Figure 5 of McDonough et al. (2023) and, under this definition, our sample contains $2,167$ high-mass galaxies and $2,709$ low-mass galaxies.

In Sections 3 and 4, we explore the role of various parameters on the radial distribution of age_L and $\Delta\Sigma_{\rm SFR}$ within galaxies. We do this by constructing radial profiles in the same manner as McDonough et al. (2023), and the reader is referred to Section 3.4 of McDonough et al. (2023) for full details of our methods. In brief, age_L profiles are constructed by directly projecting the stellar particles of each galaxy into a 2D, face-on orientation, and radial bins are normalized by the effective radius of the galaxy. A luminosity-weighted age is computed using all particles in a given radial bin for a given galaxy population. In the case of $\Delta\Sigma_{\rm SFR}$ profiles, we construct face-on maps of stellar-mass density, Σ_*, and the density of SFR, $\Sigma_{\rm SFR}$, by smoothing stellar particles onto a 2D grid using a cubic spline kernel. Maps of $\Sigma_{\rm SFR}$ are constructed using a combination of stellar particles formed in the last 20 and 100 Myr, timescales that are roughly comparable to the Hα and D4000 observational tracers of star formation. Additionally, a fixed sSFR of $10^{-12}\mathrm{yr}^{-1}$

is assumed for spatial bins where star formation was not resolved in the simulation. Finally, a map of $\Delta\Sigma_{\rm SFR}$ is constructed by determining the logarithmic offset of a given spatial bin from the resolved star-forming main sequence presented in McDonough et al. (2023). Our $\Delta\Sigma_{\rm SFR}$ profiles were constructed to be comparable to the $\Delta\Sigma_{\rm SFR}$ profiles of MaNGA galaxies presented in Bluck et al. (2020b).

In addition, we compute gradients, ∇_{1R_e}, for the profiles (which are taken to be the slope of a line fit to the profiles in the radius range $0 \leq r \leq 1R_e$), and we only present profiles for galaxy populations when there are at least 10 representative objects in our sample. We note that the aging of stellar populations that formed during the inside-out growth of galaxies can naturally result in negative gradients in age$_L$. However, the luminosity-weighting will bias the measured age$_L$ toward more recent star formation. While other works (e.g., González Delgado et al. 2016; Sánchez et al. 2021) measure gradients over different regimes and measure the profiles out to larger radii, we have here tailored our derivation of $\Delta\Sigma_{\rm SFR}$ for comparison to Bluck et al. (2020b), who used a single gradient and were limited in radial range by the coverage of the primary MaNGA sample.

While $\Delta\Sigma_{\rm SFR}$ traces star formation activity over the last 100 Myr, age$_L$ reflects both recent star formation activity (emphasized via the luminosity-weighting) and the natural aging of stellar populations. Thus, age$_L$ profiles will be useful for understanding quenching processes that operate over longer timescales, while $\Delta\Sigma_{\rm SFR}$ will be more useful for identifying parameters that contribute to rapid quenching. As reported in McDonough et al. (2023), profiles of $\Delta\Sigma_{\rm SFR}$ in galaxies undergoing active quenching are biased toward low $\Delta\Sigma_{\rm SFR}$ at intermediate radii, likely due to resolution limits imposed by the simulation.

In Appendix A, we explore the interdependence of the parameters that we discuss in this paper, and we do this separately for central and satellite galaxies. In Appendices B and C, the normalization of age$_L$ profiles are taken to be the total age$_L$ of a galaxy using all stellar particles within $1.5R_e$ and the normalization of $\Delta\Sigma_{\rm SFR}$ profiles are taken to be the logarithmic offset of a galaxy's SFR from the star-forming main sequence identified for TNG100 galaxies in McDonough et al. (2023).

2.1. *Intrinsic Parameters*

In Section 3, we present the ways in which intrinsic factors affect the radial distribution of luminosity-weighted stellar age. There we show population-averaged profiles for our sample, subdivided by supermassive black (SMBH) mass, cumulative feedback energy injected by the SMBH in the high-accretion rate ('quasar') mode, as well as the morphological Gini-M_{20} 'bulge statistic' (Snyder et al. 2015), which separates early- and late- type galaxies by quantifying the relative dominance of galaxy bulges. In addition to the results from these three parameters, we also briefly summarize results we obtain for other parameters that are related to the SMBH and morphology.

From the TNG100 `SubFind` catalog, which identifies parameters for individual subhalos (i.e., galaxies), we obtained the $z = 0$ SMBH masses, M_{BH}, and instantaneous SMBH accretion rates for our sample. Since the instantaneous accretion rate is not indicative of processes that affected the $z = 0$ radial profiles, we also obtained the SMBH accretion rate from the penultimate simulation snapshot using the `Sublink` merger trees, which corresponds to the SMBH accretion rate at redshift $z \approx 0.01$. We note that, in TNG100, black hole particles are seeded into galaxies when the halo mass exceeds $5 \times 10^{10} h^{-1} M_{\odot}$, and the galaxy does not already contain a SMBH. This black hole seeding prescription results in the majority of galaxies in our sample having SMBHs. However, a small number (107), most of which are low-mass satellite galaxies, lack SMBHs.

We obtained the cumulative feedback energy imparted by a black hole on its host galaxy, $\Sigma E_{\rm AGN}$, directly from the particle data. To do this, we identified the most massive black hole particle present within the effective radius of each galaxy in the $z = 0$ snapshot. These particles lie at the centers of the galaxies, since the TNG algorithm employs a centering prescription that ensures the SMBHs remain at the gravitational potential minima of their hosts' halos. Each black hole particle contains several tracked fields, including cumulative feedback energy injected in both the quasar mode and radio mode. The quasar (or 'thermal') mode operates when the black hole particle is in the high accretion state, and thermal energy is injected into the surrounding gas. The radio (or 'kinetic') mode operates when the particle is in the low accretion state, in which case pure kinetic energy is injected into the surrounding gas. In our sample, $3,598$ galaxies experienced energy being injected via the quasar mode ($\Sigma E_{\rm QM}$) during their lifetimes. Only 337 galaxies in our sample experienced injection of kinetic energy ($\Sigma E_{\rm RM}$) during their lifetimes. Such a low number of galaxies with non-zero values of $\Sigma E_{\rm RM}$ is not necessarily surprising since the radio mode generally takes over at low redshift in galaxies with $M_* > 10^{10.5} M_{\odot}$ (Weinberger et al. 2018). In Section 3.1, we show profiles of galaxy populations subdivided by cumulative energy imparted in the quasar mode, as that is the dominant, more energetic process. However, we also briefly discuss profiles of galaxy populations that are subdivided by cumulative energy imparted in the radio mode and the total overall energy imparted, $\Sigma E_{\rm AGN}$, where $\Sigma E_{\rm AGN} = \Sigma E_{\rm QM} + \Sigma E_{\rm RM}$.

Below, we also explore the dependence of radial profiles on morphology using the Gini-M_{20} bulge statistic. The SKIRT Synthetic Images and Optical Morphologies supplementary catalog from Rodriguez-Gomez et al. (2019) contains morphological parameters for 4999 galaxies in our sample at $z = 0$, including the bulge statistic. We also briefly discuss results using the Sérsic index (Sérsic 1963), n, which was obtained from 2D Sérsic fits to synthetic i-band images and is provided in the Rodriguez-Gomez et al. (2019) supplementary catalog.

The Gini-M_{20} bulge statistic, hereafter $F(G, M_{20})$, is defined in Snyder et al. (2015) and describes the location of a galaxy on a diagram plotting the Gini coefficient (G) against the M_{20} statistic. The Gini coefficient, traditionally used as a statistic in economics to study the distribution of wealth, was proposed as a method to measure the distribution of flux in pixels by Abraham et al. (2003) and Lotz et al. (2004). At $G = 1$, all of the flux from a galaxy is concentrated in a single pixel, while at $G = 0$, the flux is spread evenly among every pixel. M_{20} measures the second-order moment of the brightest 20% of the flux in a galaxy.

The combination of G and M_{20} into the $F(G, M_{20})$ statistic separates galaxies into early- and late- types, and indicates the relative dominance of the bulge. The greater the dominance of the bulge, the higher the value of $F(G, M_{20})$ is above zero. The more disk-dominated a galaxy is, the lower the value of $F(G, M_{20})$ is below zero. The bulge statistic is strongly correlated with other statistics that measure galactic bulge strength, including the Sérsic index and concentration. However, $F(G, M_{20})$ is less sensitive to mergers and other disturbances, making it a better indicator of bulge strength in our satellite sample.

2.2. *Environmental Parameters*

For both central and satellite galaxies, we explore the dependence of radial age$_L$ profiles on halo mass and local galaxy overdensity. We take the halo mass to be the total mass of all particles belonging to the friends-of-friends group to which a galaxy belongs. To best compare our results for simulated galaxies to the observational results obtained Bluck et al. (2020b) for observed galaxies, we evaluate the local galaxy overdensity at the fifth nearest neighbor with an absolute r-band magnitude of $M_r < -20$. The local galaxy overdensity is then computed according to:

$$\delta_5 \equiv \frac{n_5}{\bar{n}} - 1 = \frac{5}{\frac{4}{3}\pi d_5^3} \frac{L_{\text{box}}^3}{N_{\text{total}}} - 1, \tag{1}$$

where d_5 is the distance to the fifth nearest neighbor, N_{total} is the total number of TNG100 galaxies with $M_r < -20$, and L_{box} is the box length of the simulation.

2.2.1. *Satellite Parameters*

In satellite galaxies, interactions with other galaxies and with the hot gas in their hosts' halos can affect the availability of gas for star formation. It is not trivial to parameterize these interactions; e.g., the degree to which a satellite has been affected by ram pressure stripping or galaxy-galaxy harassment. However, we can quantify how properties of each satellite have changed since it joined its host's halo.

We define the satellite joining time to be the redshift at which the satellite first entered within $3R_{200}(z)$ of the center of its $z = 0$ host halo. Here, $R_{200}(z)$ is the virial radius of the host galaxy at a given redshift. To obtain the positions and properties of galaxies and their $z = 0$ groups, we used the `SubLink` merger trees of the galaxies. For the halo properties, we used the merger tree of the primary (most massive) group member at $z = 0$.

From the merger trees, we obtain the redshift at which the satellite joined (z_j), the redshift of the snapshot at which the satellite most recently approached perigalacticon (z_{p}), and the separation between the satellite and its host at perigalacticon (d_{h-s}). Additionally, we identify the total change in the mass of bound, star forming gas since the satellite joined ($\Delta M_{\rm SFG}$). The gas particle data was obtained from the satellite subhalo cutouts, from which we computed the total mass of gas particles with non-zero instantaneous star formation rates. The difference in mass from the $z = 0$ snapshot cutouts and the cutout at the snapshot corresponding to z_j then yields the values $\Delta M_{\rm SFG}$ for a given galaxy.

In Section 4, we present radial profiles of age$_L$ and $\Delta\Sigma_{\rm SFR}$ for galaxy populations subdivided by z_j and $\Delta M_{\rm SFG}$, and we briefly discuss results for $z_{\rm p}$ and d_{h-s}.

3. DEPENDENCE ON INTRINSIC PARAMETERS

3.1. *Supermassive Black Hole*

In Figures 1 and 2, we present profiles of luminosity-weighted age and $\Delta\Sigma_{\rm SFR}$, respectively, for populations of galaxies in our sample, subdivided by SMBH mass. The left panels show profiles for central galaxies, while the right panels show profiles for satellite galaxies. The top panels show profiles for galaxies with $M_* < 10^{10} M_\odot$, while the bottom panels show profiles of high-mass galaxies ($M_* > 10^{10.5} M_\odot$). The boundaries for the SMBH mass bins, the profile gradients, and the number of galaxies in a given bin are included in the legends. Error bounds (computed via 2,000 bootstrap resamplings) are indicated by shaded regions when they are larger than the line widths, and are omitted when they are comparable to or smaller than the line widths. In Figure 2, the black dashed line indicates the threshold below which $\Sigma_{\rm SFR}$ is unresolved and is therefore artificially imposed.

Purple lines in Figures 1 and 2 give the profiles for galaxies that lack SMBHs (i.e., no SMBH was seeded in these galaxies; see Section 2.1). For low-mass satellites that lack SMBHs, the age$_L$ profiles are ~ 0.5 dex (~ 500 Myr) older than the profiles of low-mass galaxies that do contain SMBHs. While there is a high degree of variability, $\Delta\Sigma_{\rm SFR}$ profiles of low-mass satellites without SMBHs appear almost completely quenched, on average. There is some evidence that ongoing star formation occurs in the centers of these galaxies, although this is not reflected in the complimentary age$_L$ profiles. The older age$_L$ and quenched $\Delta\Sigma_{\rm SFR}$ profiles of satellites without SMBHs is consistent with previous results that find that the presence of a SMBH prevents overcooling and leads to overly-efficient early star formation (e.g., Silk & Mamon 2012).

In the case of galaxies for which SMBHs were seeded, we find remarkable similarity in both shape and normalization of the age$_L$ and $\Delta\Sigma_{\rm SFR}$ profiles of low-mass galaxies with varying $M_{\rm BH}$. However, there is a clear difference in shape and normalization of profiles for high-mass galaxies with different values of $M_{\rm BH}$. That is, the more massive a SMBH, the older the age$_L$ profile and the lower the $\Delta\Sigma_{\rm SFR}$ profile. Feedback from SMBHs drives inside-out quenching (Nelson et al. 2021), which is indicated by a negative (positive) age$_L$ ($\Delta\Sigma_{\rm SFR}$) profile gradient. Of the three seeded

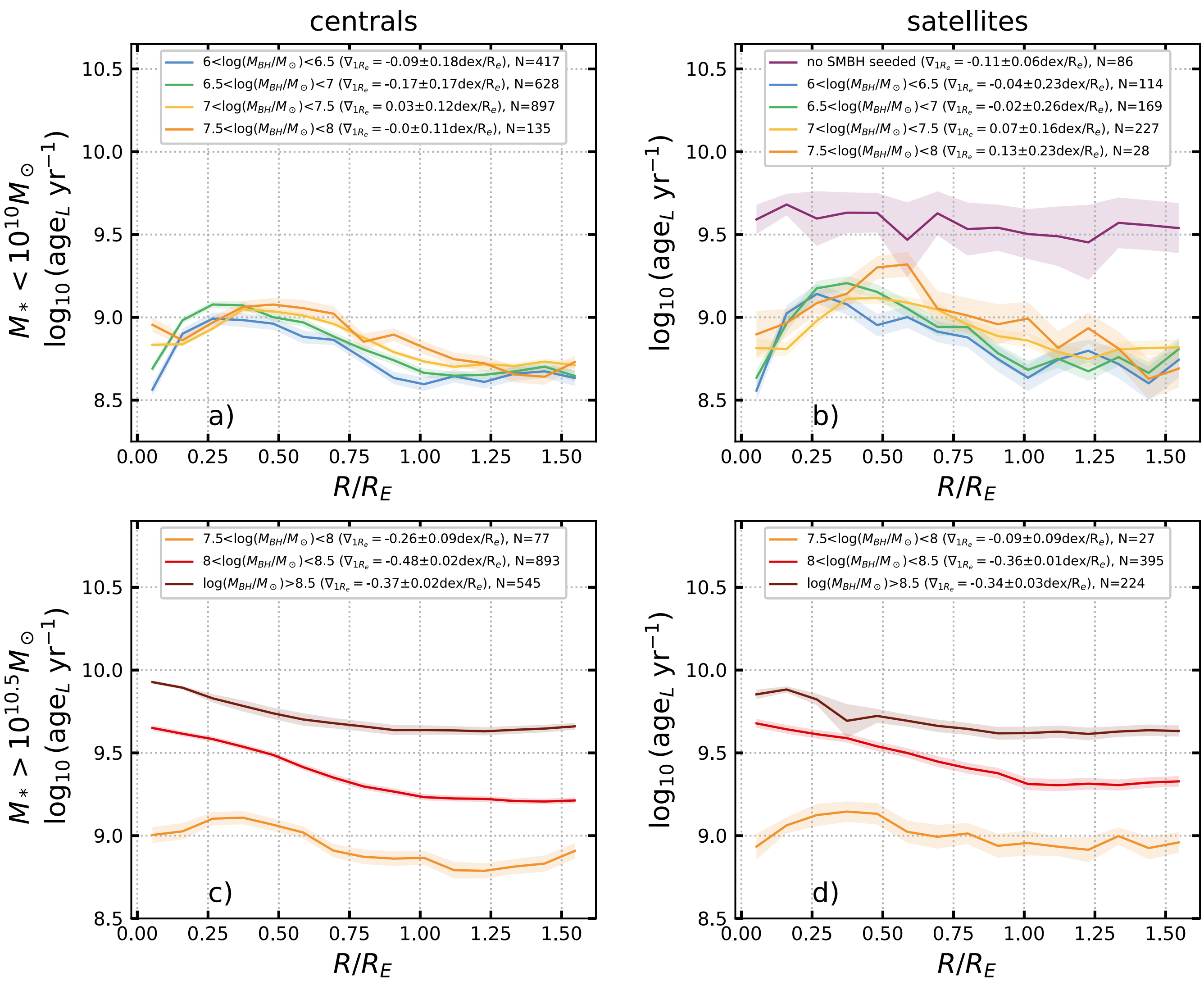

Figure 1. Radial profiles of age$_L$, subdivided by SMBH mass. The legends indicate the profile gradients (∇_{1R_e}) and the number of galaxies that contributed to the profile (N). Profiles were computed separately for populations of high-mass (top row) and low-mass (bottom row) central (left column) and satellite (right column) galaxies. Errors were computed using 2,000 bootstrap resamplings of the data. Error bounds that are wider than the line width are indicated by shaded regions and are omitted from the figure when they are comparable to or smaller than the line width.

populations of high-mass central galaxies, the middle population, $10^8 < M_{\rm BH}/M_\odot < 10^{8.5}$, has the steepest slopes ($\nabla_{1R_e}\mathrm{age}_L = -0.48 \pm 0.02$ dex$/R_e$, $\nabla_{1R_e}\Delta\Sigma_{\rm SFR} = 1.61 \pm 0.52$ dex$/R_e$).

For both high-mass centrals and satellites, the $10^{7.5} < M_{\rm BH}/M_\odot < 10^8$ (orange) population has the age$_L$ profiles with the shallowest gradient. In the $\Delta\Sigma_{\rm SFR}$ profiles (Figure 2), the profiles of high-mass galaxies with $M_{\rm BH}/M_\odot > 10^{8.5}$ (purple) are completely quenched. By construction, such low values of $\Delta\Sigma_{\rm SFR}$ are artificially imposed, so no further conclusions can be drawn from these profiles.

While not shown here, we have also explored radial profiles of galaxies subdivided by the accretion rates of their SMBHs in both the $z = 0$ snapshot and the previous snapshot, $z \approx 0.0095$. From this, we find that there is little

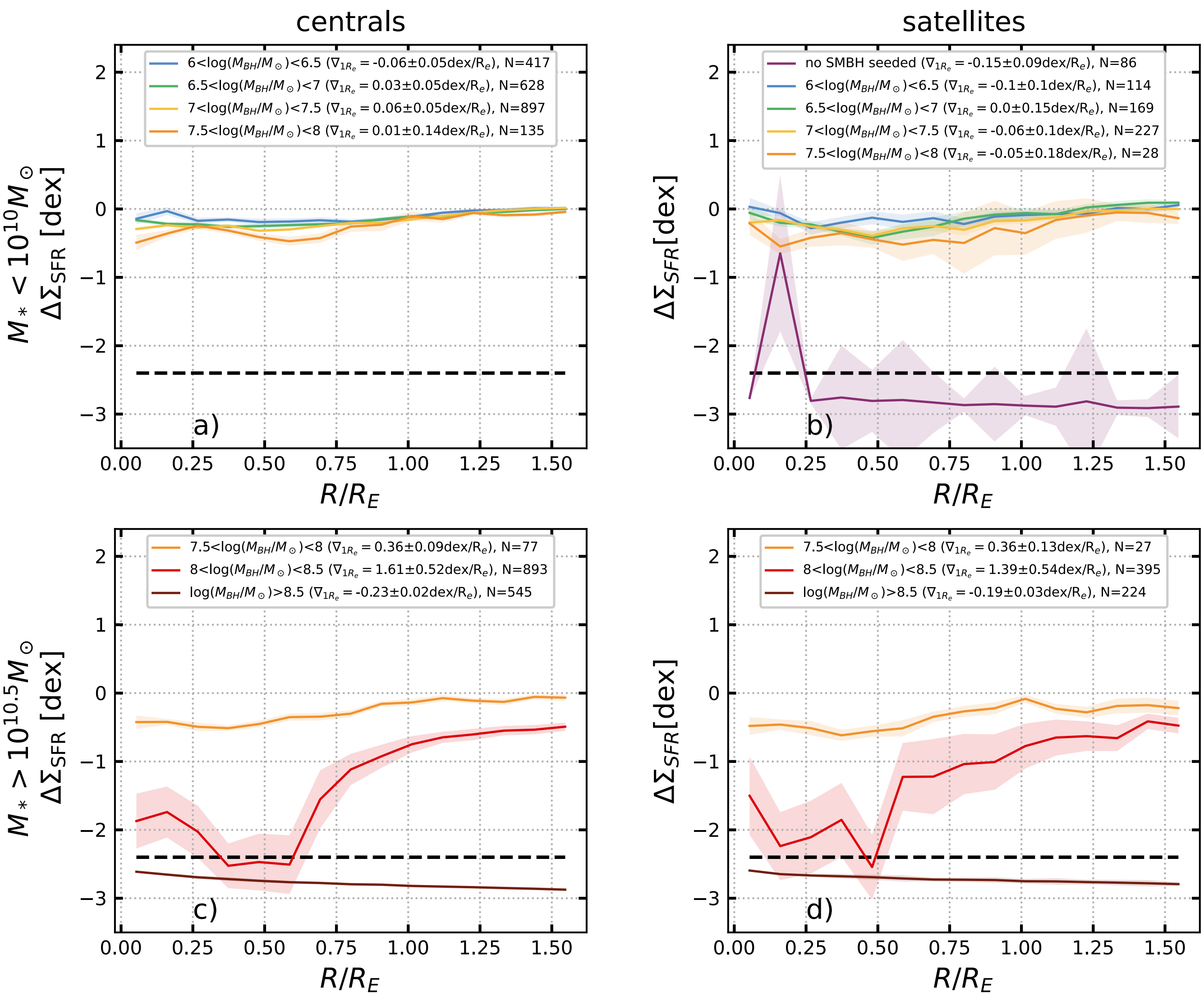

Figure 2. Radial profiles of $\Delta\Sigma_{\rm SFR}$, subdivided by SMBH mass. Here, the formatting is identical to that of Figure 1, but with the addition of a black dashed line that indicates the threshold below which a spatially resolved bin is fully quenched.

difference between profiles based on accretion rates taken at different snapshots. Similar to $M_{\rm BH}$ above, the SMBH accretion rates have little effect on the shape or normalization of radial profiles of low-mass galaxies. There is a slight exception in the $\Delta\Sigma_{\rm SFR}$ profiles of low-mass satellite galaxies with $\dot{M}_{\rm BH}^{z\approx0.01} < 10^{-5} M_{\odot}{\rm yr}^{-1}$. This population is highly variable, but on average, have lower values of $\Delta\Sigma_{\rm SFR}$ than satellites with higher accretion rates. The normalization of age$_L$ profiles of high-mass galaxies is correlated with accretion rate, but not to the same degree as profiles subdivided by $M_{\rm BH}$. These results are not surprising, as the feedback energy imparted by the accretion at $z = 0$ will not have had time to affect the galaxy, and age$_L$ will be affected by feedback that is imparted over timescales longer than the time between $z = 0$ and $z \lessapprox 0.0095$. This is consistent with the results of Bluck et al. (2023), who found that quenching

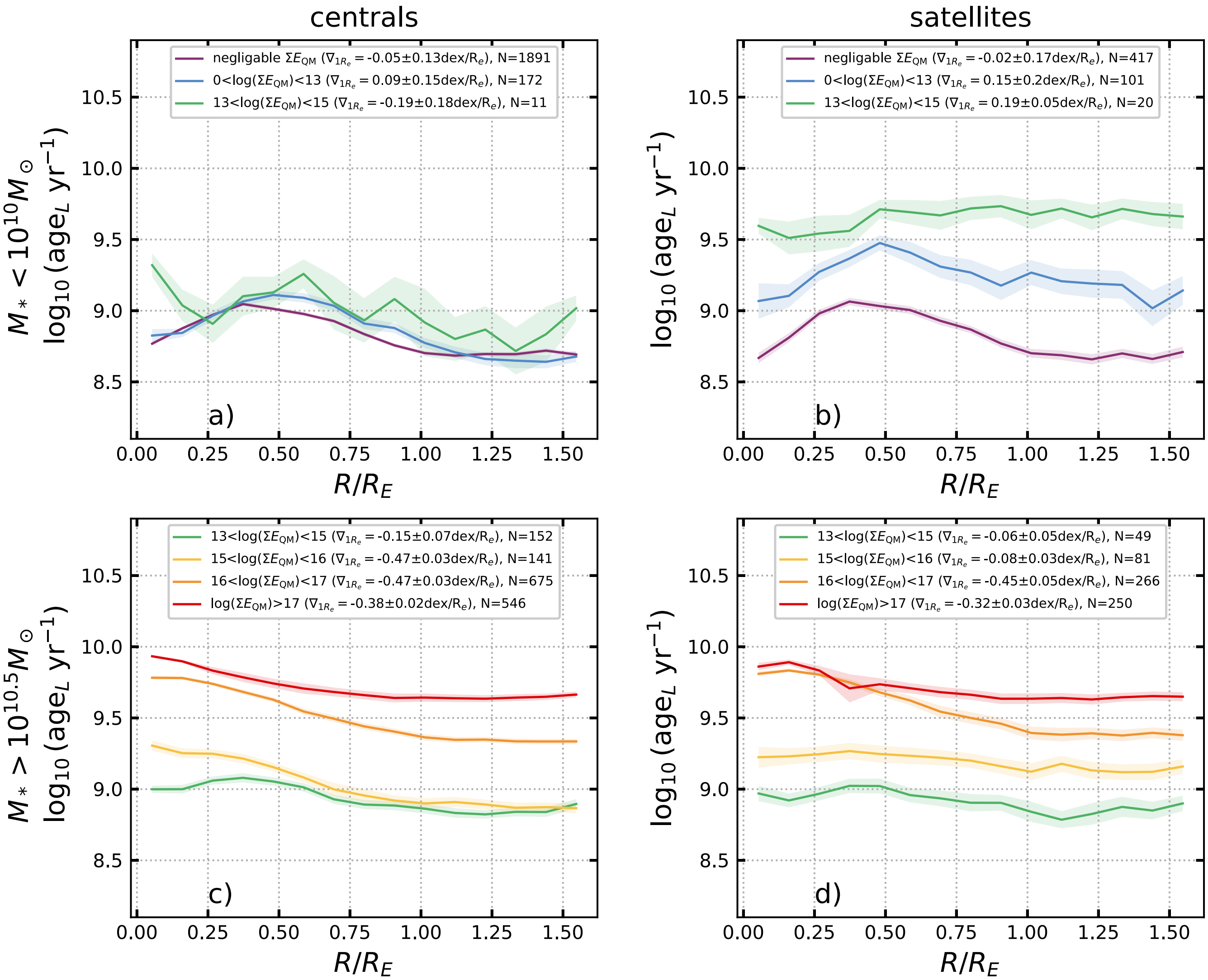

Figure 3. Radial profiles of age$_L$, subdivided by cumulative AGN feedback energy imparted in the quasar mode, $\Sigma E_{\rm QM} = \Sigma(E_{\rm QM}/(M_\odot {\rm kpc}^2{\rm Gyr}^{-2}))$, where $E_{\rm QM}$ has units of $M_\odot{\rm kpc}^2{\rm Gyr}^{-2}$. Formatting is identical to Figure 1.

of star formation showed little dependence on instantaneous SMBH accretion rate, but strong dependence on total SMBH mass.

The amount of AGN feedback energy imparted onto a galaxy at a given snapshot is proportional to the instantaneous accretion rate of the black hole. Thus, the cumulative energy imparted will be proportional to the total accretion onto the black hole over its lifetime. Since the $z = 0$ black hole mass is a summation of the matter accreted over its lifetime, $M_{\rm BH}$ and $\Sigma E_{\rm QM}$ will be well-correlated, and this is shown in Appendix A.

In Figures 3 and 4, the formatting is identical to Figure 1 and 2, except profiles are subdivided by the cumulative energy imparted by the SMBH in the quasar mode, $\Sigma E_{\rm QM}$. The units of $\Sigma E_{\rm QM}$ that we use are the reduced "code units" of $M_\odot{\rm kpc}^2{\rm Gyr}^{-2}$. For sake of brevity within the text, we do not explicitly include the units of $\Sigma E_{\rm QM}$ below.

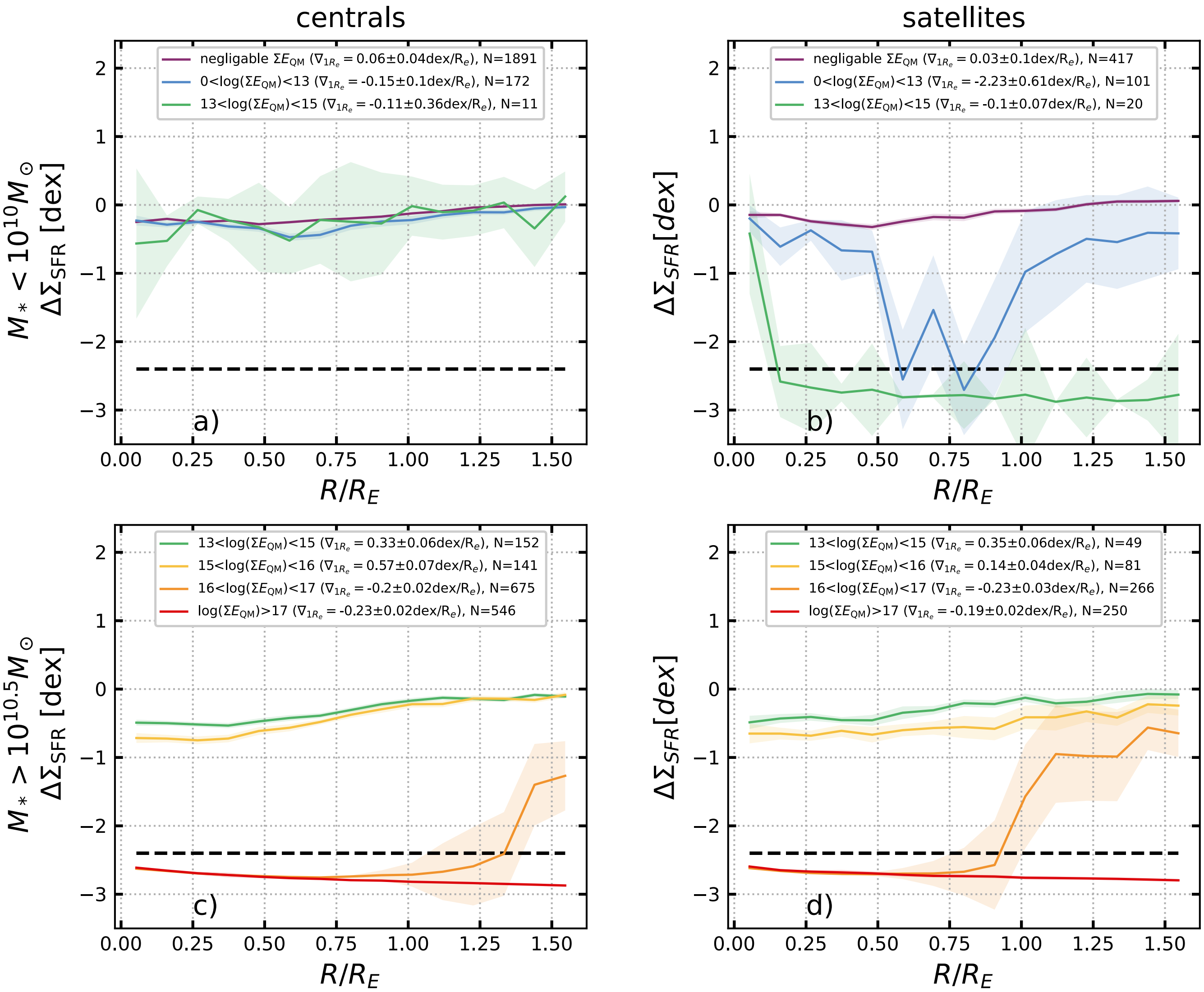

Figure 4. Radial profiles of $\Delta\Sigma_{\rm SFR}$, subdivided by cumulative AGN feedback energy imparted in the quasar mode, and corresponding to Figure 3. Here, the formatting is identical to that of Figure 2.

Figures 3 and 4 show only profiles for galaxies with seeded SMBHs, although some of these black holes have imparted negligible feedback energy. For the high-mass galaxy populations in panels c) and d), both the shape and normalization of the profiles vary with different values of $\Sigma E_{\rm QM}$. For both high-mass central and satellite galaxies, the normalization of the age$_L$ profiles increases with increasing $\Sigma E_{\rm QM}$. Notably, the steepest age$_L$ profiles for high-mass galaxies are not found in the bin with the highest $\Sigma E_{\rm QM}$, rather they are found in the intermediate bins.

In Figure 4, high-mass galaxies with the greatest $\Sigma E_{\rm QM}$ have profiles that lie entirely below the quenching threshold. While the centers of galaxies with $10^{16} < \Sigma E_{\rm QM} < 10^{17}$ (orange) are completely quenched, there is still ongoing star formation in the outskirts (at $\gtrsim 1.25 R_e$ for centrals and $\gtrsim 0.9 R_e$ for satellites.

Moving to the low-mass population, we find that $\Sigma E_{\rm QM}$ has little effect on the profiles of central galaxies. This, however, is not the case for satellite galaxies, where we find that the normalization of age_L profiles for low-mass satellite galaxies increases with increasing $\Sigma E_{\rm QM}$. The population of low-mass satellite galaxies with $10^{13} < \Sigma E_{\rm QM} < 10^{15}$ (green) have averaged $\Delta\Sigma_{\rm SFR}$ profiles that are almost entirely quenched, except at the very center. These results are somewhat surprising, since $\Sigma E_{\rm QM}$ is correlated with $M_{\rm BH}$, and the results shown in Figures 1 and 2 indicate no difference in profile normalization as a function $M_{\rm BH}$ for the low-mass satellite population.

There are only 337 galaxies in our sample with non-negligible AGN fedback energy imparted in the radio mode, ΣE_{RM}. This feedback mode only turns on at low accretion rates, typically in massive, quenched galaxies (Weinberger et al. 2018). The low number of galaxies with any ΣE_{RM} makes it impossible to draw firm conclusions about sub-populations.

Profiles of populations subdivided by total AGN feedback energy imparted in both states (not shown) appear very similar to Figures 3 and 4, although there is no longer a separation in the normalization of low-mass satellite populations. Instead, the two bins with non-negligible feedback energy both appear similar in shape and normalization to the profile for low-mass satellites with $10^0 < \Sigma E_{QM} < 10^{13}$ (blue). When looking at total feedback energy for low-mass satellites, the bin with $10^{13} < \Sigma E_{AGN} < 10^{15}$ (green) contains two distinct populations: those that injected energy primarily in the radio (kinetic) mode and those that have operated primarily in the quasar (thermal) mode. Combining these populations results in a lower overall normalization than seen in the $10^{13} < \Sigma E_{QM} < 10^{15}$ (green) low-mass satellite population.

3.2. *Morphology*

Some studies (e.g., Martig et al. 2009), have indicated that the presence of a galactic bulge can decrease star formation efficiency by stabilizing gas and thereby regulating star formation. In Figures 5 and 6, we present radial profiles of age_L and $\Delta\Sigma_{\rm SFR}$ for populations of galaxies binned by the Gini-M20 bulge statistic, $F(G, M_{20})$. A positive $F(G, M_{20})$ value indicates the presence of a bulge, with higher values corresponding to stronger bulges. For different populations of galaxies in Figure 5, there is a difference in age_L profile shape and normalization between galaxies with bulge-like morphologies (green and yellow) and those without (purple and blue). Galaxies with bulges have older ages throughout, with the exception of low-mass central galaxies at small radii.

For high-mass galaxies (bottom row, Figure 5), the age_L profiles increase in normalization with increasing $F(G, M_{20})$, but the slopes for all populations except the most bulge-like agree within 1σ for centrals and 2σ for satellites. Galaxies with $F(G, M_{20}) > 0.5$ (yellow) have shallower age_L profile gradient than galaxies with weaker bulges. In the corresponding $\Delta\Sigma_{\rm SFR}$ profiles, Figure 6 shows that the $F(G, M_{20}) > 0.5$ (yellow) population is completely quenched, while

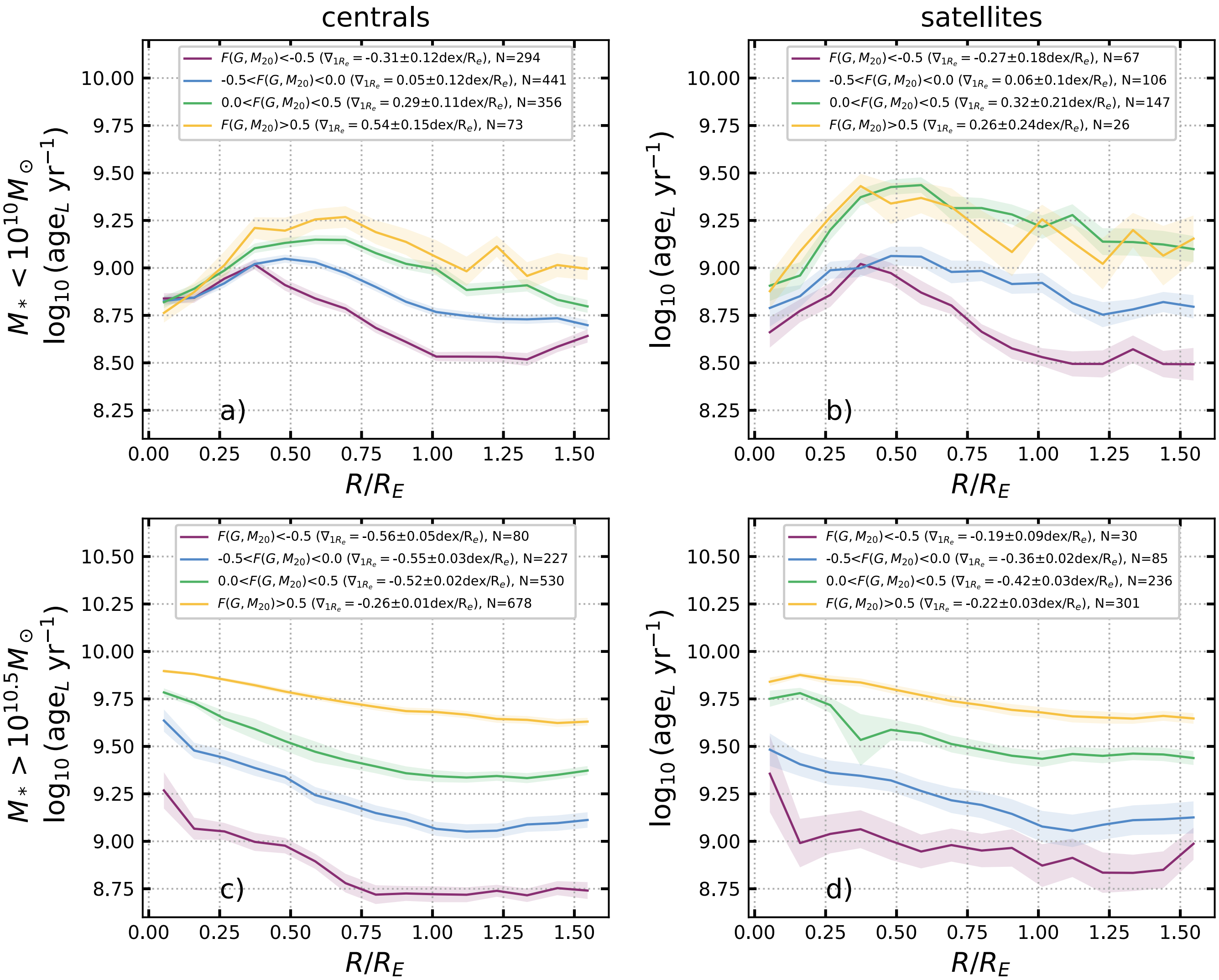

Figure 5. Radial profiles of age$_L$ subdivided by the strength of their bulge as measured by the Gini-M20 bulge statistic, $F(G, M_{20})$. Positive values of $F(G, M_{20})$ correspond to bulge-like morphology, with higher values indicating stronger bulges. Formatting is identical to Figure 1.

the $0 < F(G, M_{20}) < 0.5$ (green) population has a $\Delta\Sigma_{\rm SFR}$ profile characteristic of green valley galaxies. We note that, as shown in Appendix A, the bulge parameter is well-correlated with $M_{\rm BH}$ and $\Sigma E_{\rm QM}$.

For the low-mass galaxies (top row, Figure 5), there is a difference in the normalization of the age$_L$ profiles and, to a lesser degree, the shapes of the profiles. Bulges tend to contain older stellar populations (Sarzi et al. 2005), so the effect on the age$_L$ profiles may not reflect changes to star formation rates. Indeed, the $\Delta\Sigma_{\rm SFR}$ profiles in Figure 6 show little dependence on $F(G, M_{20})$.

At intermediate radii, $\Delta\Sigma_{\rm SFR}$ profiles of satellites with bulges ($F(G, M_{20}) > 0$) are being overwhelmed by spaxels that lack star formation, which is a known limitation in our analysis (see McDonough et al. 2023). In essence, there is a minimum resolvable star formation rate in TNG100. Resolution also limits detectable star formation levels in

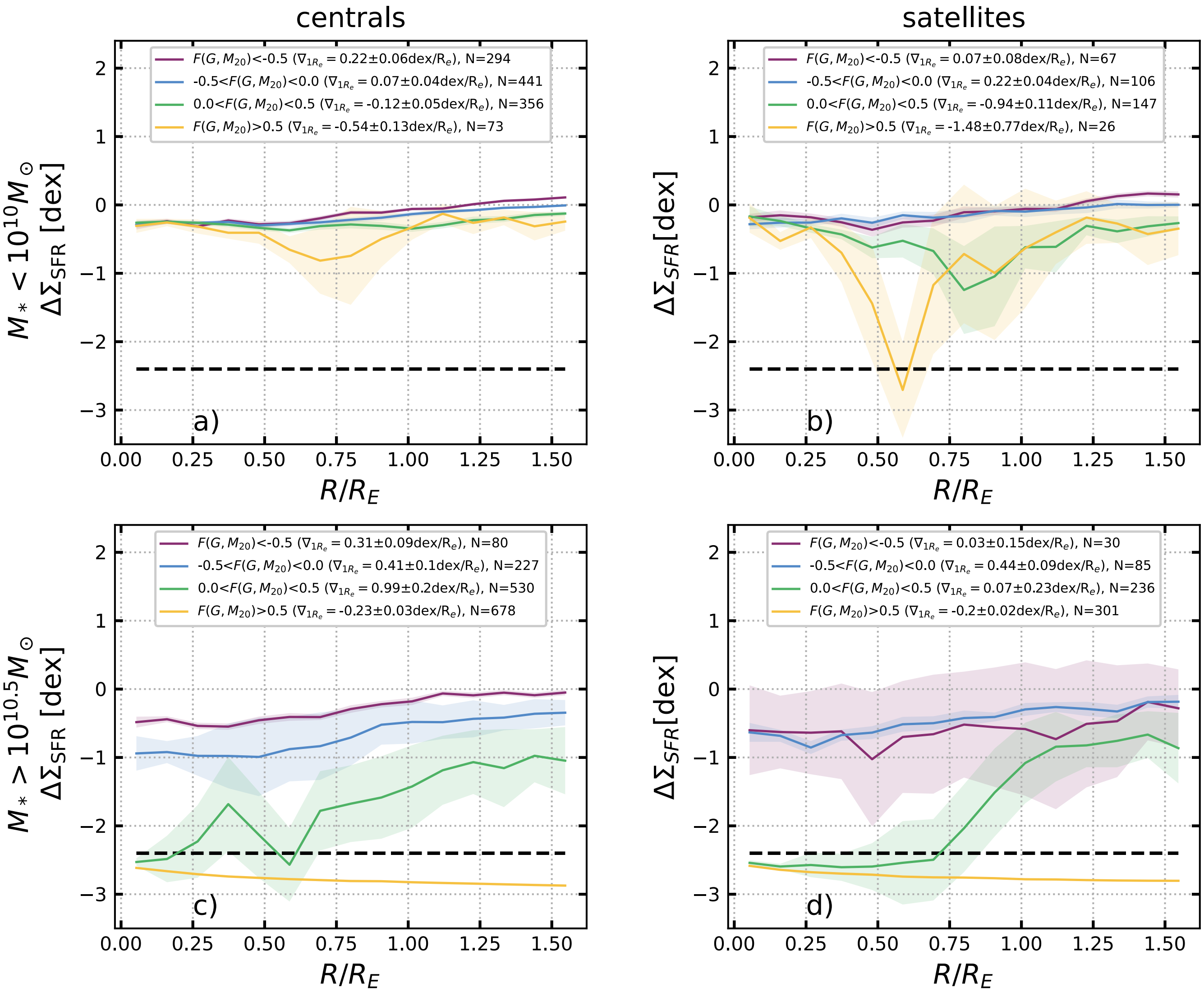

Figure 6. Radial profiles of $\Delta\Sigma_{\rm SFR}$, subdivided by the Gini-M20 bulge statistic, $F(G, M_{20})$, and corresponding to Figure 5. Here the formatting is identical to that of Figure 2.

observations. To address this, Bluck et al. (2020b) used a binning procedure that boosted the signal-to-noise, resulting in more low-SFR than high-SFR spaxels being binned together. In our analysis, we do not perform a similar binning procedure. The presence of low-$\Delta\Sigma_{\rm SFR}$ features in the top panels of Figure 6 do indicate that there is a greater percentage of quenched spaxels in those regions of bulge-like TNG100 galaxies, but we cannot draw firm conclusions about the shapes of the profiles.

We find that the age$_L$ profiles for galaxies subdivided by Sérsic indices are remarkably similar to those for the bulge statistic and we opt not to present them here. Instead, we focus on results as a function of $F(G, M_{20})$ since this parameter is better at identifying bulges in satellites that may have been disturbed by interactions (Snyder et al. 2015).

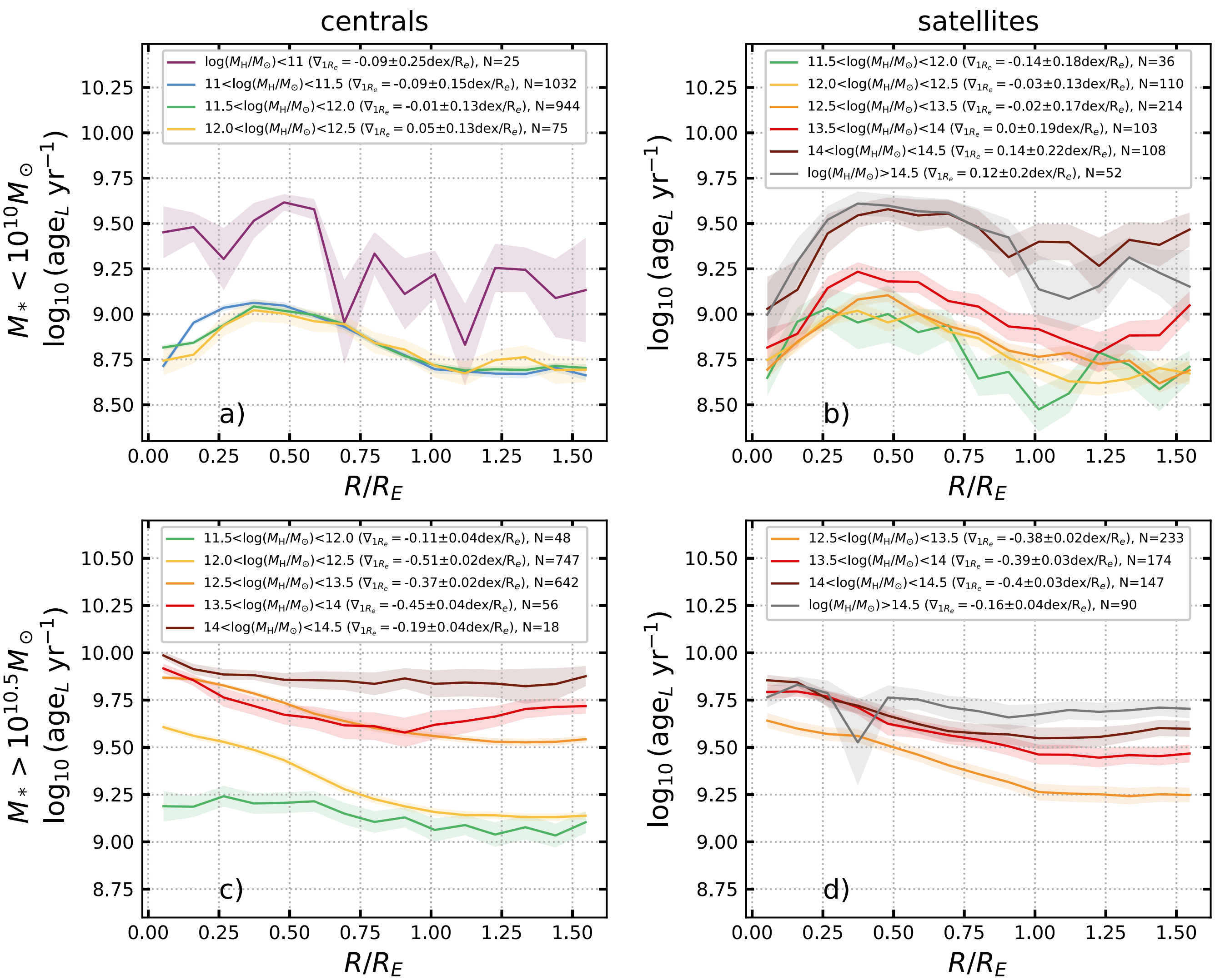

Figure 7. Radial profiles of age_L subdivided by halo mass, M_H. Formatting is identical to Figure 1.

4. DEPENDENCE ON ENVIRONMENTAL PARAMETERS

4.1. *Halo mass*

In Figures 7 and 8 we present the dependence of the distribution of age_L and $\Delta\Sigma_{\mathrm{SFR}}$ on halo mass. For the central galaxy population, halo mass scales with SMBH mass and, thus, ΣE_{QM} (see Appendix A). As in §3.1, there is little difference in normalization or shape in the profiles of the low-mass central population when subdivided by halo mass, except at the very lowest masses ($M_H/M_\odot < 10^{11}$, purple). For high-mass centrals, all populations have negative age_L gradients that are indicative of inside-out quenching, although the gradient is significantly shallower for galaxies in halos with $M_H/M_\odot < 10^{12}$ and $M_H/M_\odot > 10^{14}$. The slope of the age_L profile of central galaxies in halos with $10^{13.5} < M_H < 10^{14}$ (red) becomes positive at large radii ($\gtrsim 1R_e$), deviating from the flat outskirts seen in the other

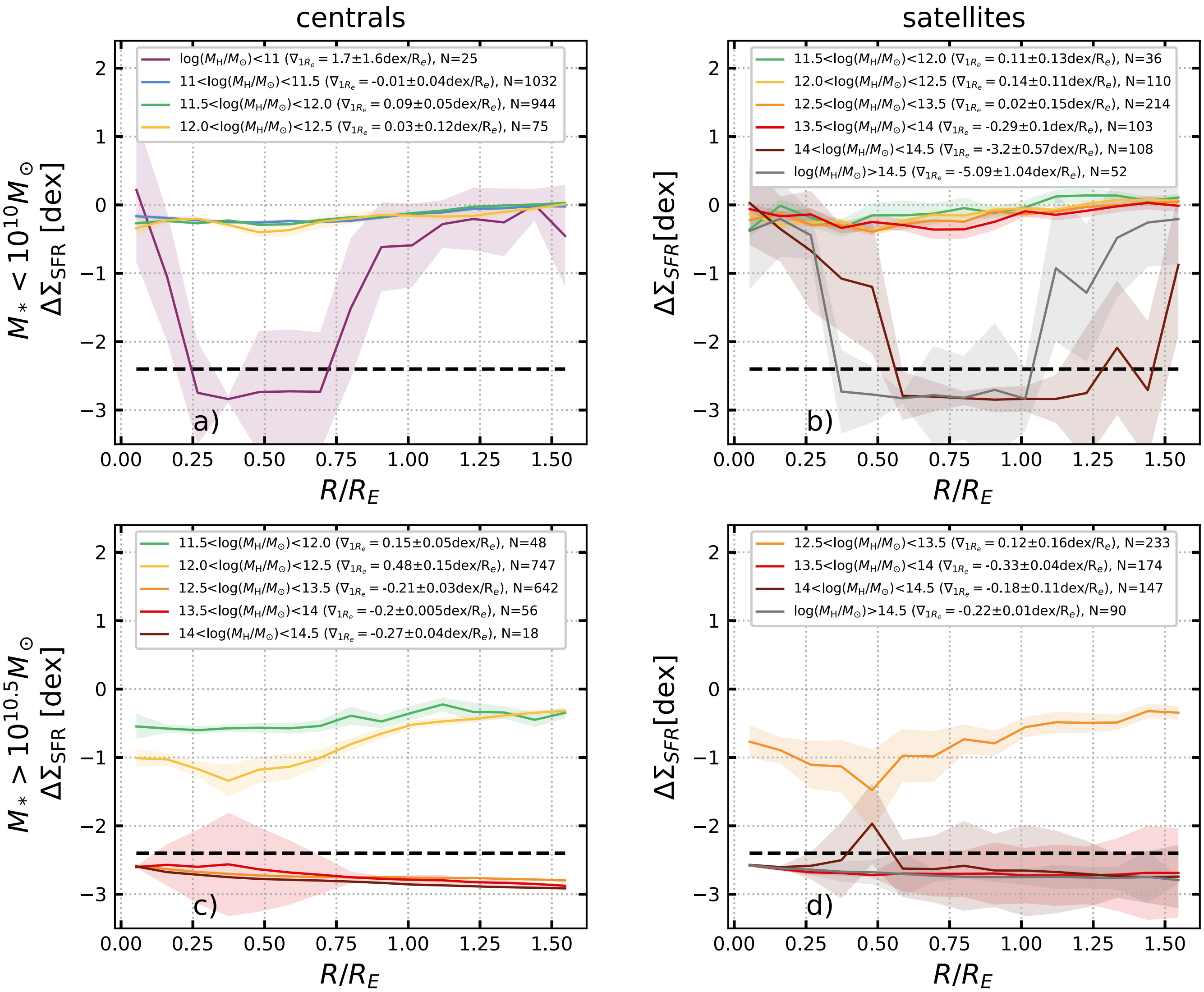

Figure 8. Radial profiles of $\Delta\Sigma_{\rm SFR}$, subdivided by host halo mass, and corresponding to Figure 7. Here the formatting is identical to Figure 2.

high-mass central populations. In Figure 8, the high-mass central population with $M_H/M_\odot > 10^{12.5}$ have average $\Delta\Sigma_{\rm SFR}$ profiles that lie entirely below the quenching threshold.

In Figure 7, both high- and low-mass satellite galaxies that reside in high-mass halos ($M_H > 10^{13.5}$) have older overall age$_L$ profile normalizations than do satellites residing in halos with $M_H < 10^{13.5}$. The difference is much larger for low-mass satellites than it is for high-mass satellites, especially at $M_H/M_\odot > 10^{14}$. At radii $> 1.25R_e$, the slopes of the profiles for low-mass satellites with $10^{13.5} < M_H/M_\odot < 10^{14}$ (red) and $10^{14} < M_H/M_\odot < 10^{14.5}$ (brown) become positive. Similar to the high-mass centrals, the age$_L$ profiles for high-mass satellites become flatter at high halo masses, although this occurs at higher halo masses for the satellites.

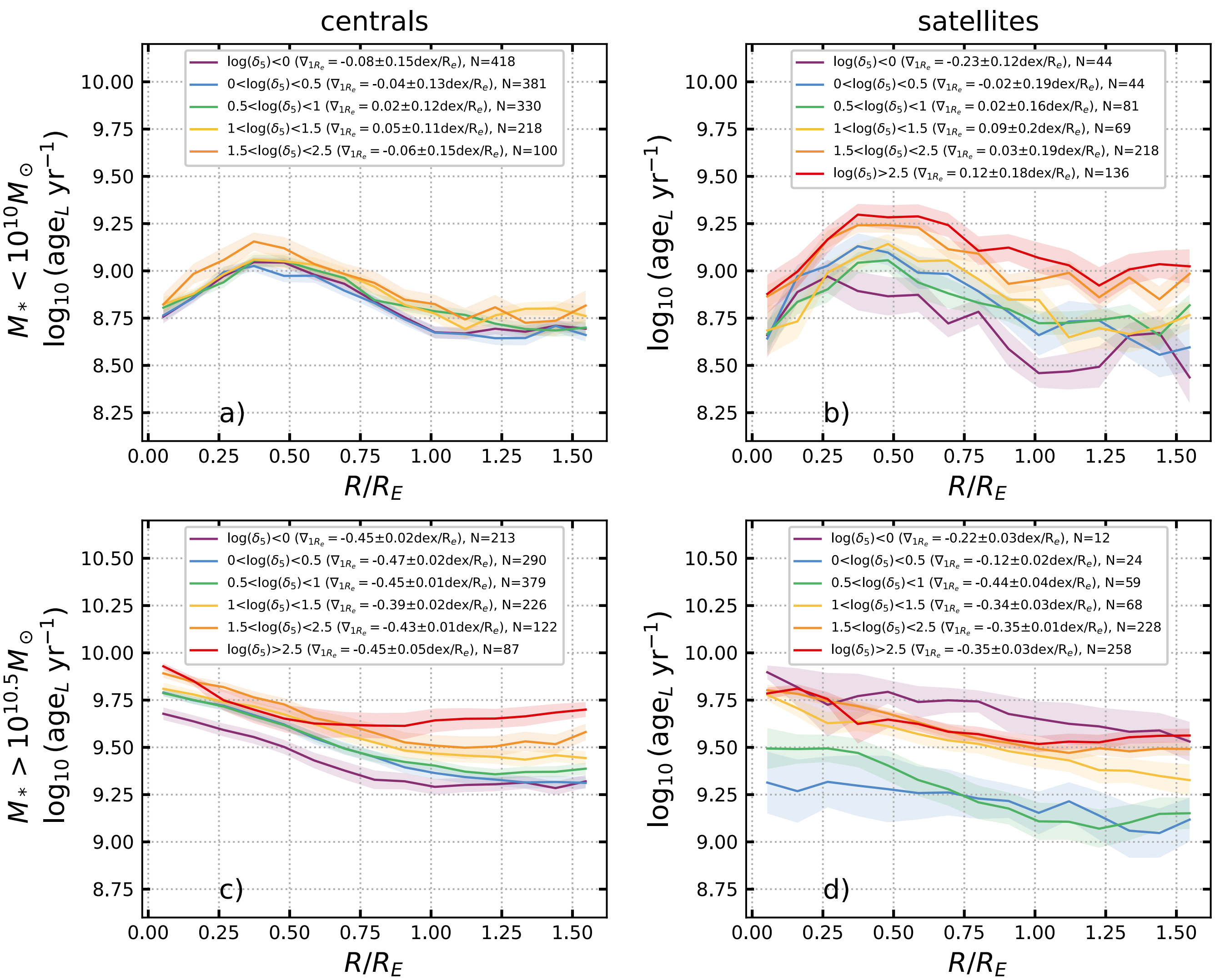

Figure 9. Radial profiles of age_L subdivided by local galaxy overdensity (see text). Formatting is identical to Figure 1.

The low-mass satellite galaxy populations with high halo masses ($M_H/M_\odot > 10^{14}$ in Figure 8b) are highly variable and suffer from the issues with low-$\Delta\Sigma_{\rm SFR}$ profiles discussed above and in McDonough et al. (2023). We caution against over-interpreting these profiles, however we can conclude that this population has a higher percentage of quenched spaxels than populations at lower halo masses. The high-mass satellites in Figure 8d) are also highly variable, resulting in large error bars. On average, high-mass satellites in halos with $M_H/M_\odot > 10^{13.5}$ are almost entirely quenched.

4.2. *Local Galaxy Overdensity*

Figures 9 and 10 present age_L and $\Delta\Sigma_{\rm SFR}$ profiles of TNG100 galaxies subdivided into populations based on local galaxy overdensity measured at the 5$^{\rm th}$ nearest neighbor. For low-mass central galaxy populations, there is very little deviation in the profiles of age_L and $\Delta\Sigma_{\rm SFR}$ over a large range of δ_5. In the case of high-mass central galaxies, the age_L profiles show slight differentiation in the normalization as a function of δ_5, although not to the same degree as

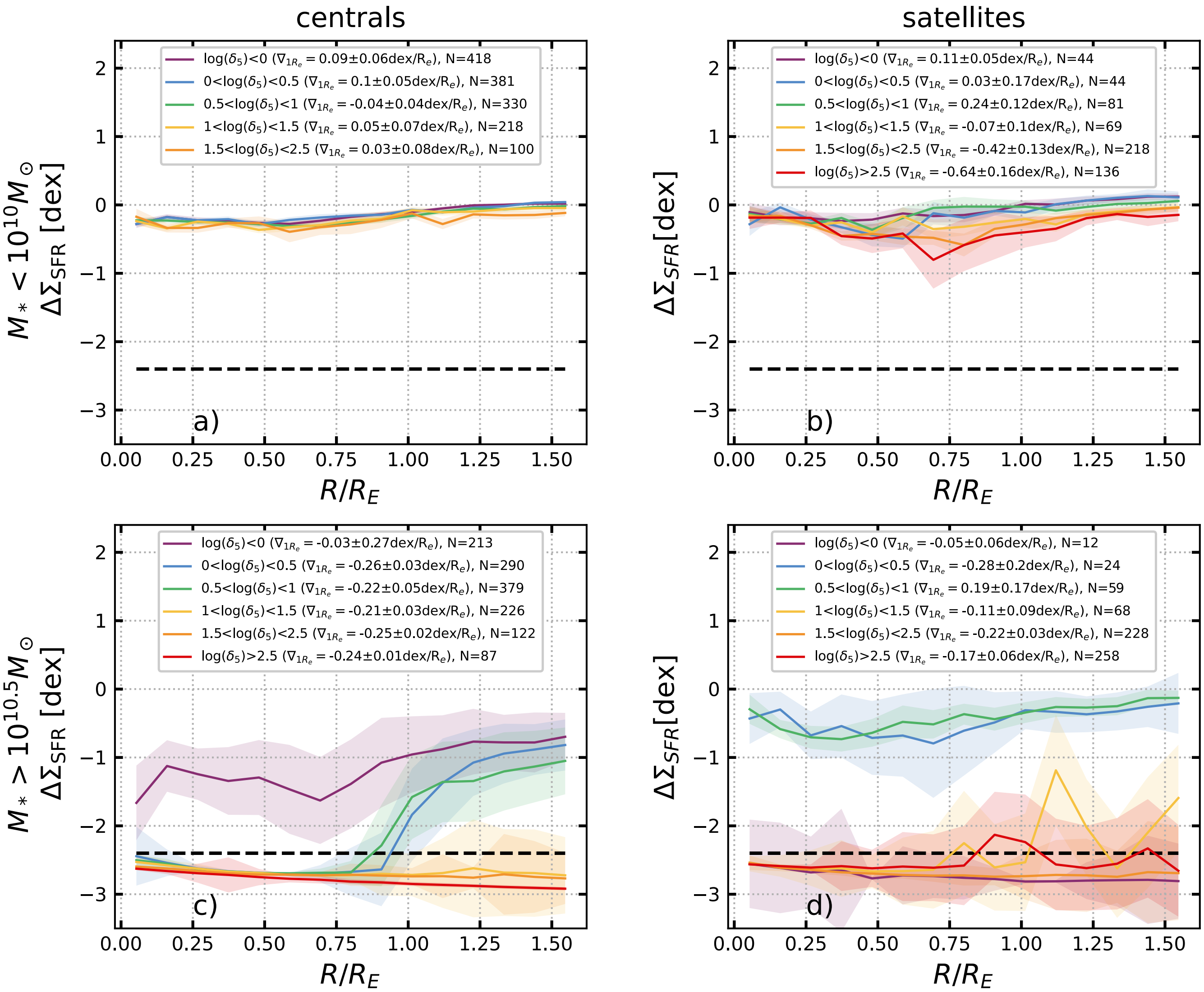

Figure 10. Radial profiles of $\Delta\Sigma_{\rm SFR}$, subdivided by local galaxy overdensity measured at the fifth nearest neighbor, that correspond to Figure 7. Here the formatting is identical to that of Figure 2.

we found above for halo mass. However, the shapes of age$_L$ profiles for high-mass galaxies with $10^{1.5} < \delta_5 < 10^{2.5}$ (orange) have a slightly positive slope in the average profile at large radii. The slope becomes more positive in the outskirts of the high-mass central population in even denser regions ($\delta_5 > 10^{2.5}$, red). Compared to other populations, high-mass central galaxies in very underdense regions ($\delta_5 < 10^0$, purple) have younger ages at $R_e < 1.0$ and they are the only high-mass central population that is still star forming throughout in Figure 10c).

In contrast, the few satellite galaxies that are found in the most underdense regions have the oldest ages and are quenched throughout, comparable to satellites in the most overdense regions. Aside from high-mass satellites in very underdense regions, there is a weak trend of increasing normalization of age$_L$ with increasing δ_5 for satellites. This trend is weaker in the $\Delta\Sigma_{\rm SFR}$ profiles, although low-mass satellites in especially overdense regions have somewhat

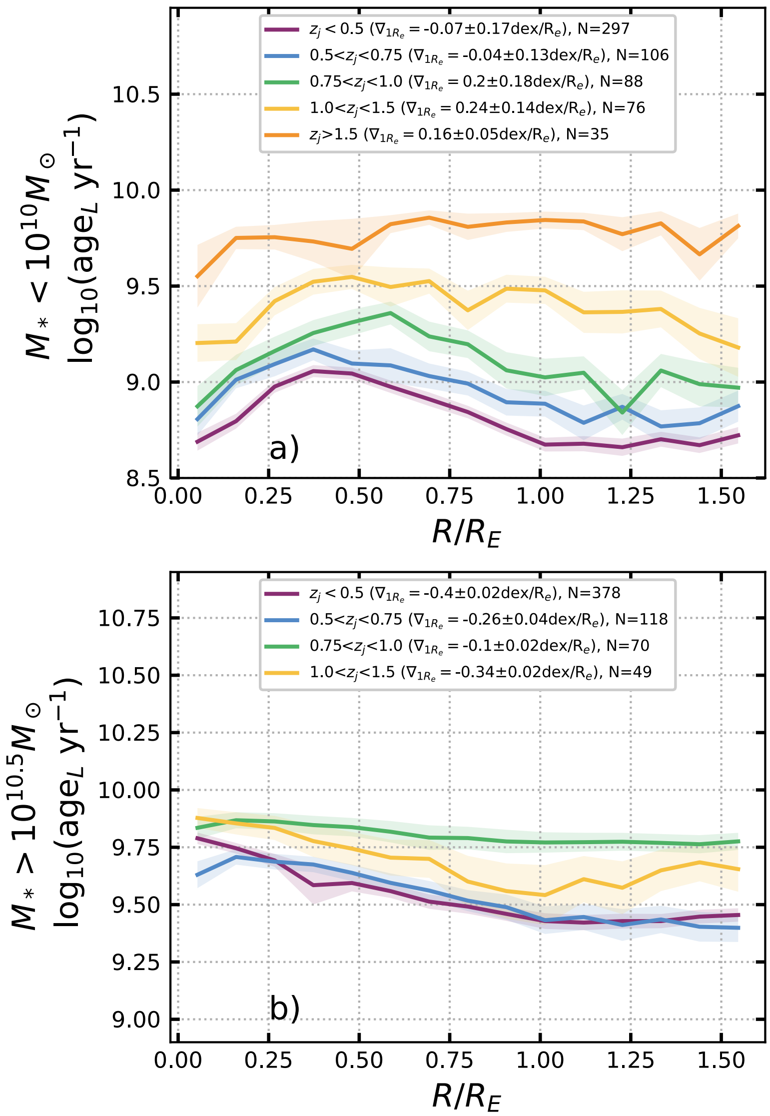

Figure 11. Radial profiles of age_L subdivided by the redshift at which the satellite entered within $3R_{200}$ of its $z = 0$ host, z_j. Formatting is identical to the right column of Figure 1.

lower SFRs at some radii. The widths of the error bars on profiles of populations subdivided by δ_5 are generally larger than those of populations subdivided by M_{H}, indicating greater variability in the profiles of individual satellites in the δ_5 populations.

4.3. *Satellite Parameters*

4.3.1. *Joining time*

The environmental processes that affect star formation in satellite galaxies are expected to scale with time spent in the host halo. More time spent in the halo will lead to a higher probability of interactions and more time for gas to be stripped from the satellite.

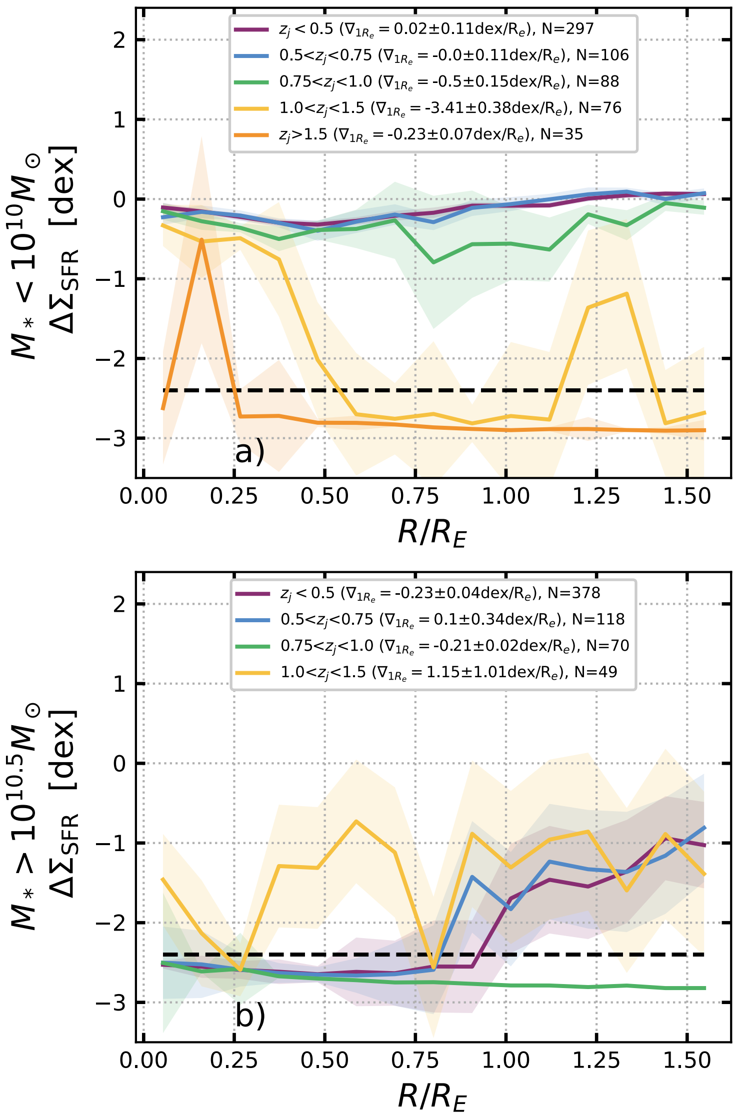

Figure 12. Radial profiles of $\Delta\Sigma_{\rm SFR}$, subdivided by the redshift at which the satellite approached within $3R_{200}$ of its $z = 0$ host, z_j, and corresponding to Figure 11. Here the formatting is identical to the right column of Figure 2.

In Figures 11 and 12, we present radial profiles of age$_L$ and $\Delta\Sigma_{\rm SFR}$ for satellites, with the sample subdivided based on the redshift at which the satellites joined their hosts, z_j. The low-mass population shows that the overall age$_L$ increases for satellite populations with greater z_j. Low-mass satellites with $z_j > 1.0$ have lower $\Delta\Sigma_{\rm SFR}$ profiles than satellites that joined later. On average, low-mass satellites with $z_j > 1.5$ only maintain some star formation in their centers.

For the high-mass galaxies, there is a curious reversal in overall age between satellites in the $0.75 < z_j < 1.0$ (green) and $1.0 < z_j < 1.5$ (yellow) populations, with the population that joined earlier having a younger overall age$_L$. This is also reflected in the $\Delta\Sigma_{\rm SFR}$ profiles, with the $1.0 < z_j < 1.5$ population maintaining some degree of star formation

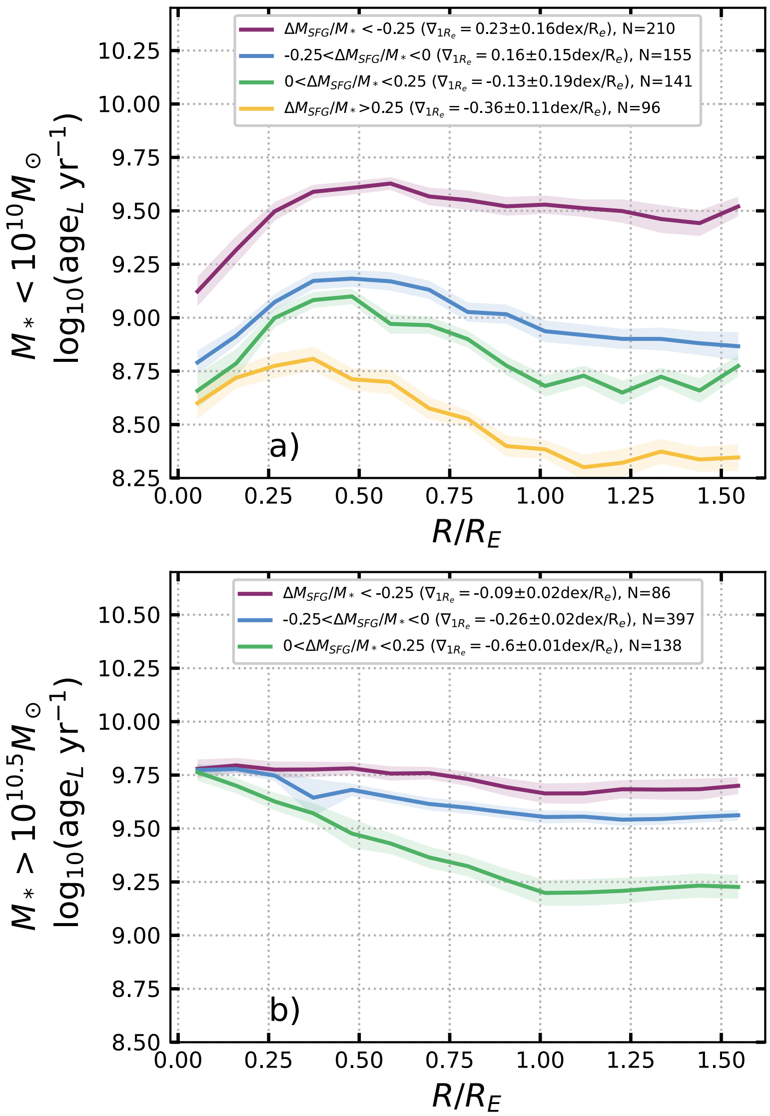

Figure 13. Radial profiles of age_L subdivided by the change in star-forming gas since the satellite entered within $3R_{200}$ of its $z = 0$ host, $\Delta M_{\rm SFG}$. Formatting is identical to Figure 11. Note that the ordinates of each panel have slightly different numerical ranges.

while the $0.75 < z_j < 1.0$ population appears entirely quenched. High-mass satellites with relatively late joining times ($z_j < 0.75$) have the characteristic inside-out age_L and $\Delta\Sigma_{\rm SFR}$ profile shapes.

Compared to more recently accreted low-mass satellites, low-mass satellites with $z_j > 1.0$ have age_L profiles that are flatter beyond $R > 0.75R_e$. High-mass satellites with $z_j > 0.75$ have flat age_L profiles. The shapes and normalizations of these profiles indicate that more outside-in quenching has operated on satellite populations that have spent longer in their hosts' environment, as expected. However, there is a high degree of variation within a given population, as indicated by the shaded error bars.

4.3.2. *Change in mass of star forming gas*

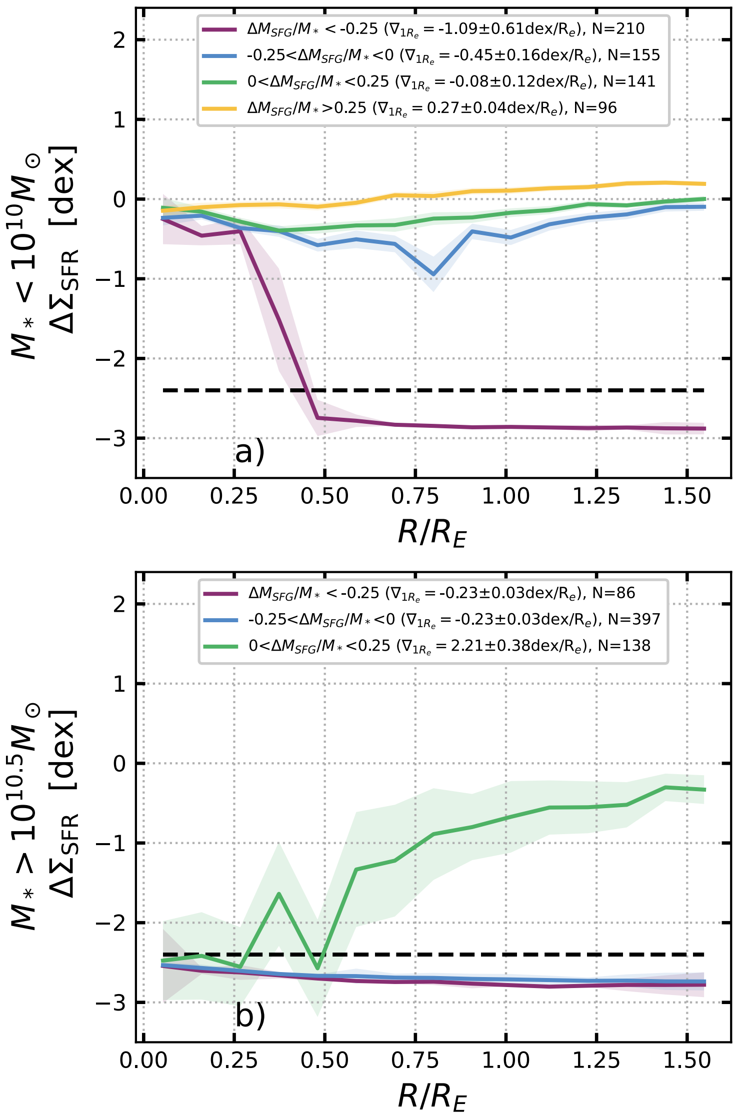

Figure 14. Radial profiles of $\Delta\Sigma_{\rm SFR}$, subdivided by the change in star-forming gas since the satellite approached within $3R_{200}$ of its $z = 0$ host, and corresponding to Figure 11. Here the formatting is identical to the right column of Figure 2.

Any process that affects star formation in galaxies affects the availability of star-forming gas (SFG). In the simulation, it is possible to determine the change in star-forming gas since a satellite joined the host halo, $\Delta M_{\rm SFG}$. In Figures 13 and 14, we present radial profiles of age$_L$ and $\Delta\Sigma_{\rm SFR}$ subdivided by $\Delta M_{\rm SFG}$, and normalized by the stellar mass of each satellite. For low- and high-mass satellites, there is a clear offset in overall age and $\Delta\Sigma_{\rm SFR}$ for different bins of $\Delta M_{\rm SFG}$. Satellites that, proportionately, have lost more star-forming gas are systematically older and have lower $\Delta\Sigma_{\rm SFR}$, while those that have gained star-forming gas are systematically younger and have higher $\Delta\Sigma_{\rm SFR}$. For low-mass galaxies, the difference in age$_L$ for satellites with $\Delta M_{\rm SFG}/M_* < -0.25$ and satellites with $\Delta M_{\rm SFG}/M_* > 0.25$ is nearly 3 Gyr (~ 1 dex). While low-mass satellites with significant SFG loss maintain typical levels of star formation at their centers ($R < 0.25R_e$), at radii $> 0.5R_e$ they are completely quenched.

There are no high-mass satellite galaxies that have gained more than 25% of their stellar mass in star-forming gas. The age difference between high-mass satellites with $\Delta M_{\rm SFG}/M_* < -0.25$ (purple) and high-mass satellites that have gained any star-forming gas is about 3.5 Gyr (~ 0.5 dex) in the outskirts. The high-mass satellites with positive $\Delta M_{\rm SFG}$ (green) are the only population of high-mass satellites that show significant levels of star formation, which is occurring at radii $> 0.5R_e$.

There is a clear difference in age$_L$ profile shape for satellites that have gained star-forming gas and those that have lost star-forming gas. Satellites with negative $\Delta M_{\rm SFG}$ are older than satellites with positive $\Delta M_{\rm SFG}$, particularly in the outskirts ($R \gtrsim 0.5R_e$). These results demonstrate that the change in the availability of star-forming gas is occurring in the outskirts of these simulated galaxies, consistent with outside-in quenching or enhancement.

4.3.3. *Perigalacticon*

For each satellite in our sample, we obtained the redshift at which it last made its closest approach, $z_{\rm p}$, as well as the closest approach the satellite made to its host, d_{h-s}. Here, we briefly summarize the age$_L$ and $\Delta\Sigma_{\rm SFR}$ profiles of galaxy populations subdivided by these parameters, although we refrain from showing them since, for the most part, the differences are relatively minor.

There is no significant dependence of age$_L$ profile on d_{h-s} for high-mass satellite galaxies. For low-mass satellites, significant differences only appear for satellites with $d_{h-s} < 0.5R_{200}$. The outskirts of low-mass satellites with $d_{h-s} < 0.5R_{200}$ are ~ 0.4 dex (~ 550 Myr) older than satellites with $d_{h-s} > 2R_{200}$. There is no significant trend in outskirt ages when finer bin sizes are used to define populations at smaller host-satellite separations. The corresponding $\Delta\Sigma_{\rm SFR}$ profiles are very noisy, indicating a high degree of variability among the individual galaxy profiles. Profiles of low-mass satellites are nearly identical. There is no significant trend with d_{h-s} for high-mass galaxies, with most profiles appearing entirely quenched or indicative of typical inside-out quenching. The only exception is the profile of satellite galaxies with the smallest perigalacticon separation, $d_{h-s} < 0.1R_{200}$. This profile is quenched in the center and outskirts, but maintains active star formation at $0.5 \lesssim R/R_e \lesssim 1.2$. However, this is one of the noisiest profiles, with errors in the range of $\sigma_{\Delta\Sigma_{\rm SFR}} \approx 0.75 - 0.95$ at $R/R_e > 0.5$.

For $z_{\rm p}$, the age$_L$ profiles of low-mass satellites have a normalization trend that is similar to that of populations subdivided by z_j (Figure 11), with satellites with larger values of $z_{\rm p}$ having older ages. Satellites with $z_{\rm p} > 0.5$ have the oldest ages and flatter age$_L$ profiles. The trend in increasing age$_L$ normalization with increasing $z_{\rm p}$ is weaker for high-mass satellites than it is for low-mass satellites. Satellites with $z_{\rm p} > 0.1$ have ages that are ~ 0.2 dex (~ 1.8 Gyr) older than satellites with the latest perigalacticon approaches. This is a significantly smaller difference than satellites with the earliest and latest z_j, which is ~ 0.5 dex (~ 5 Gyr).

The $\Delta\Sigma_{\rm SFR}$ profiles subdivided by $z_{\rm p}$ are very noisy. The profiles correspond well with insights gleaned from the complimentary age$_L$ profiles. Low-mass satellites with $z_{\rm p} > 0.5$ are the only low-mass satellite population with a profile that lies below the quenching threshold at any radius ($R/R_e > 0.3$). The high-mass satellite profiles are indicative of active inside-out quenching, with the exception of the population with $z_{\rm p} > 0.1$, which is entirely quenched.

It is not surprising that satellite populations with the earliest perigalacticon approaches are quenched, as these populations also have the earliest joining times. However, the reverse is not necessarily true, as satellites with early joining times may have relatively recent perigalacticon approaches. The noisiness of the age$_L$ and $\Delta\Sigma_{\rm SFR}$ profiles, along with the relatively weak trends with d_{h-s} and $z_{\rm p}$, lead us to believe that these parameters play a relatively minor, if any, role in quenching satellites.

5. DISCUSSION

In this paper, we have considered various parameters that are related to the two main quenching processes identified in the literature: mass quenching and environmental quenching.

In the mass quenching scenario (see, e.g., Peng et al. 2010; Ma et al. 2022; Bluck et al. 2020b), energy from the central supermassive black hole acts on gas from the interstellar and circumgalactic media, preventing further accretion and star formation. The exact mechanism by which the SMBH affects star formation is still unclear, but it may be a combination of heating, removal, or the introduction of turbulance that decreases star formation efficiency. The degree to which AGN feedback negatively affects star formation in a galaxy increases with increasing amounts of energy imparted by the black hole. This process is known as mass quenching because the energy scales with black hole mass and, thus, stellar mass. Mass quenching operates at stellar masses greater than $\sim 10^{10} M_\odot$ (e.g., Bluck et al. 2020b; McDonough et al. 2023).

Intrinsic feedback processes in low-mass galaxies are not powerful enough to quench these systems, but do act to slow the natural exhaustion of their gas reservoirs, which generally allows these systems to maintain star formation at present-day. Other processes must be necessary to quench galaxies at low masses, since quenched galaxies at $M_* \lessapprox 10^{10} M_\odot$ do exist. These low-mass, quenched galaxies consist primarily of satellite galaxies that reside in group and cluster environments, where environmental processes are common. Environmental quenching is any external process that negatively affects the availability of star forming gas in a galaxy, and is particularly important for satellites (see, e.g., Peng et al. 2012; Bluck et al. 2020a; Bluck et al. 2020b; Corcho-Caballero et al. 2023).

As mass quenching is the dominant process in high-mass galaxies, defined as $M_* > 10^{10.5} M_\odot$ in this paper, we will discuss our results for high-mass and low-mass ($M_* < 10^{10} M_\odot$) galaxies separately.

5.1. *High-mass galaxies*

In Figures 1 and 3 (bottom panels), mass quenching is clearly operating in both high-mass central and satellite galaxies. More massive black holes and higher values of $\Sigma E_{\rm QM}$ correlate with older ages, as expected. This correlation is the result of star-formation quenching and natural aging processes (since progenitors of the most massive galaxies would have formed early according to hierarchical structure formation). The slopes of the age$_L$ profiles are negative.

Negative age$_L$ gradients are to be expected to some degree, as galaxies grow from the inside-out (e.g., Sánchez et al. 2021), with stellar populations forming first near the center before star formation progresses to the outskirts. However, the gradients of the age$_L$ and $\Delta\Sigma_{\rm SFR}$ profiles in Figures 1-4 become steeper as $M_{\rm BH}$ and $\Sigma E_{\rm QM}$ increase, except at the highest bin. Galaxies with the most massive black holes and highest imparted energies have older, flatter age$_L$ profiles and are completely quenched in the $\Delta\Sigma_{\rm SFR}$ profiles. Since the brightest stars in a stellar population age and die quicker than dimmer populations, age$_L$ will increase faster in regions where star formation has been quenched more recently as compared to the age$_L$ of stellar populations that have been quenched for some time. This results in a flattening of the age$_L$ profiles once star formation in the outskirts quenches. Our results indicate that the degree of inside-out quenching increases as $M_{\rm BH}$ and $\Sigma E_{\rm QM}$ increase, up to $M_{\rm BH}/M_\odot \approx 10^{8.5}$ and $\Sigma E_{\rm QM} \approx 10^{17}$, at which point the galaxy is completely quenched.

This interpretation is supported by the distributions of main sequence, green valley, and quenched galaxies in these parameters, which are shown in Appendix A. Figures 17 and 18 show that very few main sequence galaxies have values of $M_{\rm BH}$ and $\Sigma E_{\rm QM}$ greater than the stated thresholds.

We note that there is some disagreement between our $\Delta\Sigma_{\rm SFR}$ profiles in Figure 2 and those obtained from MaNGA observations by Bluck et al. (2020b). They found that central galaxies with $M_{BH}/M_\odot > 10^{6.5}$ were, on average, quenched at small radii. In contrast, we only see significantly quenched centers for TNG100 galaxies with central black hole masses $M_{BH}/M_\odot < 10^8$. This disagreement of 1.5 orders of magnitude in SMBH mass for central quenching could be the result of a number of factors, including sample properties, comparability of M_{BH} measurements in simulations and observations, or limitations with how black holes and feedback are modeled in the simulation. Despite quantitative disagreement, we find the same general trend as Bluck et al. (2020b) in the TNG100 high-mass central galaxies, with evidence for more inside-out quenching as black hole mass increases.

In the case of intrinsic parameters, it is challenging to disentangle the relative effects of mass and morphology on the distribution of star formation. The presence of a bulge correlates with the mass of a galaxy, which correlates with the star formation properties of a galaxy. Thus, the fact that galaxies in Figure 5c,d) with $F(G, M_{20})> 0.5$ (yellow) have older age$_L$ profiles may just be an indication that this population is, on average, more massive. There is generally more variability in the age$_L$ and $\Delta\Sigma_{\rm SFR}$ profiles when galaxies are binned by $F(G, M_{20})$ than by $M_{\rm BH}$ or $\Sigma E_{\rm QM}$. This indicating that mass rather than morphology likely drives quenching in high-mass TNG100 galaxies.

Environmental quenching is not the dominant quenching process for high-mass galaxies, especially central galaxies. However, there are clear effects on the luminosity-weighted age in the outskirts of high-mass galaxies that reside in extreme environments. In Figure 7(c), central galaxies with $M_H/M_\odot < 10^{13.5}$ have flat age$_L$ profiles in the outskirts. At slightly higher halo masses, $10^{13.5} < M_H/M_\odot < 10^{14}$ (red), the age$_L$ profile slope for central galaxies becomes positive in the outskirts ($R > 1R_e$). The slope in the inner regions is still negative, indicating that this population is being quenched inside-out and outside-in. In the next highest halo mass bin, $10^{14} < M_H < 10^{14.5}$ (brown), the profile for central galaxies is significantly flatter and older throughout than central galaxies with $10^{13.5} < M_H/M_\odot < 10^{14.5}$ (red). In Figure 8, the $\Delta\Sigma_{\rm SFR}$ profiles of high-mass, central galaxy populations with $M_H/M_\odot > 10^{12.5}$ are completely quenched, the same threshold identified by Bluck et al. (2020b) for all central galaxies. For high-mass satellites, the halo mass threshold for quenching in Figure 8d is $M_H/M_\odot > 10^{13.5}$. This is slightly lower than the threshold identified by Bluck et al. (2020b) ($M_H/M_\odot > 10^{14}$), although this threshold was determined with profiles constructed by satellite galaxies of all masses in their sample.

Since halo mass is correlated with black hole mass for central galaxies, it is instructive to compare age$_L$ profiles at high M_H with profiles at high M_{BH}. The typical galaxy with $M_{BH}/M_\odot > 10^{8.5}$ is completely quenched, and the age$_L$ profile (Figure 1c) shows that this occurred through inside-out quenching. The population of galaxies with $10^{14} < M_H/M_\odot < 10^{14.5}$ (brown) is also completely quenched, but the inner gradient of the average age$_L$ profile ($\nabla_{1R_e} = -0.19 \pm 0.04$ dex/R$_{\rm e}$) is much less negative than the same gradient for the $M_{BH}/M_\odot > 10^{8.5}$ (Figure 1c, brown) population ($\nabla_{1R_e} = -0.37 \pm 0.02$ dex/R$_{\rm e}$).

High halo masses (at $M_H/M_\odot \gtrsim 10^{13.5}$) are also correlated with high local galaxy overdensity. In the highest bin of δ_5 that we include (Figure 9c, red), the slope of the age$_L$ profile for high-mass central galaxies becomes positive at $R \gtrsim 0.6R_e$. This population is entirely quenched in profiles of $\Delta\Sigma_{\rm SFR}$ (Figure 10). The correlation between M_H and δ_5 makes it difficult to ascertain which mechanisms − interactions with the hot gas halo or interactions with other galaxies − are acting to quench the outskirts of these systems.

Similar trends are present, but less pronounced, for high-mass satellite galaxies that reside in similar environments (Figures 7d and 9d). This may be due to the fact that some satellites in the most massive halos, or with the largest values of δ_5, may have joined the system only recently. For high-mass satellites with $M_H/M_\odot > 10^{13.5}$, the age$_L$ profiles are similar at $R \lesssim 0.5R_e$, but the outskirts become older with increasing halo mass. The slopes of the age$_L$ profiles of high-mass satellites with $\delta_5 > 10^{1.5}$ become slightly positive at $R \gtrsim 1.1R_e$. The $\Delta\Sigma_{\rm SFR}$ profiles of high-mass satellites subdivided by δ_5 are very noisy (Figure 10d), but appear mostly quenched at $\delta_5 > 10^{1.5}$. In Bluck et al. (2020b), $\Delta\Sigma_{\rm SFR}$ profiles of high-mass satellite galaxies are completely quenched at $\delta_5 > 10^1$. Additionally, we find that high-mass TNG100 satellites in the most underdense regions ($\delta_5 < 10^0$, purple) are completely quenched, while

MaNGA satellites in similar regions maintain star formation throughout. We note that our threshold for high-mass galaxies is higher than that of Bluck et al. (2020b), which defined high-mass satellites to have $M_*/M_\odot > 10^{10}$. We further discuss the tension between our results and that of Bluck et al. (2020b) for satellites subdivided by δ_5 in the following subsection.

The radial profiles of age$_L$ for high-mass galaxies, subdivided by M_H and δ_5, indicate that environmental quenching can operate on these systems, suppressing star formation from the outside-in. At the masses and densities where environmental quenching affects the age$_L$ profiles, galaxies are already completely quenched in the $\Delta\Sigma_{\rm SFR}$ profiles. While extreme environments can contribute to the quenching of high-mass galaxies, the dominant quenching pathway for high-mass galaxies is via AGN feedback energy, as we conclude above.

In Appendix A, we provide further evidence that environmental processes are not the dominant quenching process for high-mass satellite galaxies. However, environment can still impact the evolution of these systems. High-mass satellites that joined their central galaxies at earlier times have age$_L$ profiles that are generally older and flatter than those for satellites that at joined later times, although the population with $1.0 < z_j < 1.5$ (yellow) is a curious exception in both age$_L$ and $\Delta\Sigma_{\rm SFR}$ profiles. High-mass satellites that have lost any amount of star-forming gas since joining are, on average, completely quenched. The age$_L$ profiles of these systems have negative gradients, indicating that the quenching was driven by the central SMBHs. Profiles of age$_L$ for the population of high-mass satellite galaxies that have gained star-forming gas also show evidence of inside-out quenching (Figure 13b, green), but the outskirts are significantly younger than populations with negative $\Delta M_{\rm SFG}$. It is clear, especially when considering the corresponding profiles of $\Delta\Sigma_{\rm SFR}$ in Figure 14, that the enhancement of star-forming gas has operated from the outside-in.

To summarize this section, the radial profiles of high-mass galaxies are primarily shaped by mass-quenching operating inside-out. However, environmental processes can affect the shape of age$_L$ profiles and contribute to quenching at large radii in extreme environments.

5.2. *Low-mass galaxies*

The typical age$_L$ profile for low-mass TNG100 galaxies appears similar to the age$_L$ profile for disk-dominated galaxies with $10^{9.2} < M_*/M_\odot < 10^{10.2}$ observed by CALIFA by González Delgado et al. (2014), including the dip in age$_L$ at the center. From visual inspection of maps of $\Sigma_{\rm SFR}$ in low-mass galaxies, active star formation in the center of these galaxies is common. This is generally not reflected in profiles of $\Delta\Sigma_{\rm SFR}$ and sSFR in this work and observational analysis, likely due to the relatively high stellar mass density at the centers of galaxies. Further exploration of star formation in the centers of low-mass galaxies is desirable, especially since AGN feedback in the TNG simulations is imparted at the centers of galaxies. However, such explorations are limited by resolution in both simulations and observations.

Both simulated and observed low-mass galaxies have shallower profiles than corresponding high-mass galaxies, indicating less influence by the SMBH. The age_L and $\Delta\Sigma_{\mathrm{SFR}}$ gradients that are present reflect the natural growth of the galaxies and the aging of their stellar populations. There is no significant difference in age_L or $\Delta\Sigma_{\mathrm{SFR}}$ profile shape or normalization between simulated low-mass galaxy populations over two magnitudes of black hole mass ($10^6 < M_{BH}/M_\odot < 10^8$).

There is no age_L or $\Delta\Sigma_{\mathrm{SFR}}$ profile dependence on ΣE_{QM} for simulated low-mass central galaxies, with a slight exception for galaxies with $10^{13} < \Sigma E_{QM} < 10^{15}$ at small radii. For low-mass satellite galaxies, however, there is a clear difference in normalization. In Figure 4, satellite galaxies with $10^{13} < \Sigma E_{QM} < 10^{15}$ (green) are entirely quenched except at the smallest radii. Central galaxies with comparable ΣE_{QM} are still forming stars at the same $\Delta\Sigma_{\mathrm{SFR}}$ as central galaxies with negligible ΣE_{QM}, albeit with greater variation. There is no compelling reason to expect that the same amount of AGN energy imparted into a satellite galaxy would quench the satellite but not a central of similar mass. It may be that this is a matter of correlation, rather than causation.

It is unclear what role a bulge-like morphology plays in quenching or regulating star formation in low-mass TNG100 galaxies. As discussed above, the strong correlation of $F(G, M_{20})$ with other galaxy parameters complicates this investigation. There is certainly a dependence on $F(G, M_{20})$ for age_L profiles of TNG100 galaxies, but this is not fully reflected in the $\Delta\Sigma_{\mathrm{SFR}}$ profiles in Figure 6. The flatter shapes of the age_L profiles of low-mass galaxies with $F(G, M_{20}) > 0$ are likely driven by the aging of stellar populations in the bulge, especially since there are not significant differences in the $\Delta\Sigma_{\mathrm{SFR}}$ profiles of low-mass galaxies separated by $F(G, M_{20})$. There is evidence from observations that environmental effects, particularly ram pressure stripping, can drive morphological transformation as well as the availability of star-forming gas in satellite galaxies (e.g., Steyrleithner et al. 2020; Marasco et al. 2023). Thus, morphology may not drive star formation properties, but could be affected by the same evolutionary processes.

As quenching in low-mass TNG100 galaxies is not being driven by intrinsic factors, we therefore turn to environmental processes to explain the quenched low-mass galaxies in our sample. Here, we categorize galaxies into star-forming type in the same way as in McDonough et al. (2023). Quenched galaxies are those that are ≥ 1.1 dex below the star-formation main sequence on a $M_* - \mathrm{SFR}$ diagram. We can expect differences in central and satellite galaxy quenching due to the different environmental effects these systems will experience. The likelihood of galaxy-galaxy interactions for both central and satellite galaxies will increase with increasing local galaxy density. However, only satellite galaxies will experience significant galaxy-halo interactions along their orbits within the gas halos.

The age_L profiles of low-mass central galaxies, subdivided by M_H and δ_5, deviate only slightly from each other at high halo masses and local galaxy overdensities (Figures 7a and 9a). The only exception is for central galaxies with $M_H/M_\odot < 10^{11}$ (purple), which are significantly older than central galaxies in higher mass halos. In total,

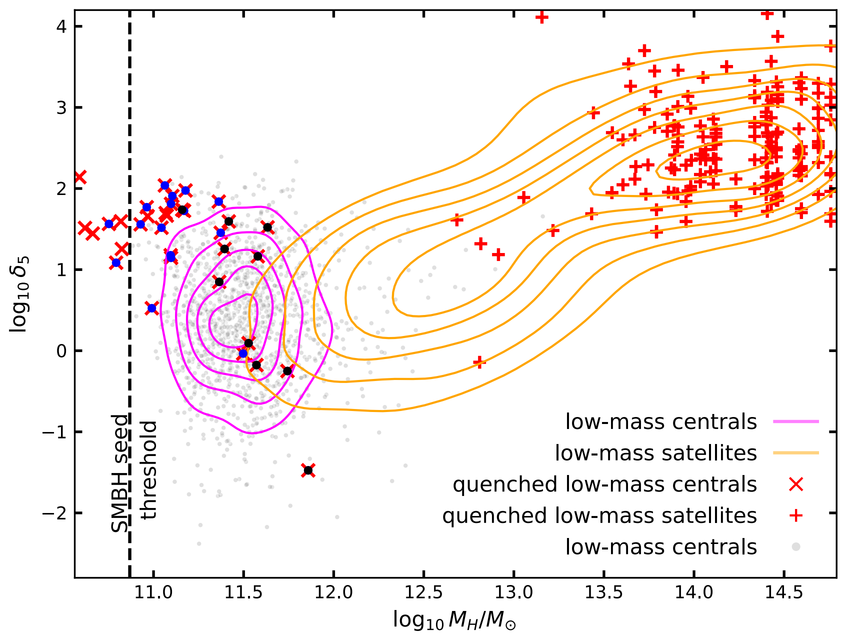

Figure 15. Comparison of the distribution of quenched low-mass central and satellite galaxies to the entire population of low-mass central and satellite galaxies. Magenta and orange contours indicate the density of the entire low-mass central and satellite population, respectively. All individual low-mass central galaxies are plotted as grey points. Quenched low-mass central galaxies are indicated as red crosses and quenched low-mass satellite galaxies are indicated as red plus signs. Low-mass, quenched centrals are overplotted with a blue dot if they contain any SMBH and a black dot if they contain an SMBH with ten times the SMBH seed mass. The black dashed line indicates the halo mass threshold for SMBH seeding.

there are 40 low-mass, quenched, central galaxies in our sample. The median values of M_H and δ_5 for the population of low-mass, quenched centrals ($\log_{10} M_H/M_\odot = 11.14$, $\log_{10} \delta_5 = 1.52$) differ from those of all low-mass centrals ($\log_{10} M_H/M_\odot = 11.49$, $\log_{10} \delta_5 = 0.405$).

In Figure 15, we draw contours around the density of low-mass central (magenta) and satellite (orange) galaxies in the $M_H - \delta_5$ parameter space. Quenched central (crosses) and satellite (plus signs) galaxies are individually plotted in red. The halo mass threshold for SMBH seeding in TNG100 is shown as a black dashed line. A blue point is overplotted on points representing quenched, low-mass centrals that contain any SMBH, and black points are plotted for quenched, low-mass centrals with SMBHs that are more than ten times the SMBH seed mass. The majority of quenched low-mass centrals lie outside the density contours for the population of all low-mass centrals and are biased toward low halo masses. However, their quiescence in TNG100 is likely due to lacking an SMBH, at least until recent times. Without an SMBH to regulate star formation through AGN feedback, these systems over-efficiently convert gas to stars throughout their early lives and are quiescent at late times.

There are a small number of low-mass, quenched centrals with more typical halo masses that have an SMBH that is more than ten times the TNG100 SMBH seed mass, meaning that the SMBHs have been accreting for some time. With such a small sample and without further analysis of these systems, it is impossible to determine how these systems became quiescent. One possibility is galaxy-galaxy interactions that can either efficiently strip gas from a system or trigger a starburst phase, during which a galaxy consumes most of its available gas over a short period of time, leading to a post-starburst quiesence (e.g., Wilkinson et al. 2021). The likelihood of such interactions is expected to scale with local galaxy overdensity, and thus the fraction of low-mass centrals that are quenched should increase with increasing δ_5. However, our sample is too small to perform such an analysis.

Unlike central galaxies, there is no correlation between M_H and stellar mass for satellite galaxies (i.e., here M_H is the mass of the halo within which the satellite is orbiting). However, interactions with the hosts' hot gas halo and host halo potential, such as ram pressure stripping and dynamical friction, should scale with halo mass (e.g., Woo et al. 2015; Bluck et al. 2016). The age$_L$ profiles of simulated, low-mass satellite galaxies in the most massive halos ($M_H > 10^{13.5} M_\odot$) and the most overdense regions ($\delta_5 > 10^{1.5}$) have higher normalizations than the age$_L$ profiles of low-mass satellites in less massive halos and less overdense regions. This is especially prominent in the profiles of populations subdivided by halo mass (Figure 7b), where satellites in halos with $M_H/M_\odot > 10^{14}$ are ~ 0.5 dex older at $R \gtrsim 0.25 R_e$ than satellites in $M_H/M_\odot < 10^{13.5}$ halos. In Figure 8b), the only low-mass satellite galaxies that are quenched at any radii are those with $M_H/M_\odot > 10^{14}$. This threshold is the same as that identified by Bluck et al. (2020b) for MaNGA satellites, although they found that low-mass satellites at halo masses greater than this threshold had $\Delta\Sigma_{\rm SFR}$ profiles that were entirely quenched. Bluck et al. (2020b) also found that the $\Delta\Sigma_{\rm SFR}$ profiles of satellites are systematically higher than those for central galaxies at all halo masses. We do not find this to be the case for TNG100 satellites once the satellites are subdivided by stellar mass.

It has been shown previously in observations that the quenched fraction of satellite galaxies increases with local galaxy overdensity and halo mass (e.g., Bluck et al. 2016, 2020a). In Figure 15, we show that quenched, low-mass satellites generally reside well within the distribution of all low-mass satellites, although they are clustered at the high M_H end of the distribution. When subdivided by δ_5, we find that there are no populations of low-mass satellite galaxies where the average $\Delta\Sigma_{\rm SFR}$ profiles have any quenched regions. This is in tension with Bluck et al. (2020b), which found that low-mass satellites at $\delta_5 > 10^{1.5}$ have $\Delta\Sigma_{\rm SFR}$ profiles that lie completely below the quenching threshold, but there are several caveats to this comparison. There are resolution limitations in how galaxy-galaxy interactions are modeled in the simulation (see, e.g., Sparre & Springel 2016). Additionally, there are also differences in how local galaxy overdensity is measured: in this work, δ_5 is measured with 3D positions, while observations are limited by the 2D view of the sky.

The longer a satellite spends in a halo, the more time there is for environmental interactions to take place, which motivates our investigation of the dependence of radial profiles on z_j. In Figure 11 (top), low-mass satellites that joined their hosts' halos earlier have, on average, older age_L than systems that joined their hosts' halos only recently. In Figure 12, we see that only the populations of low-mass satellite galaxies that joined earlier than $z = 1$ are, on average, almost completely quenched. Additionally, beyond $R \approx 0.5R_e$, the age_L profiles of these early joiners are flatter than they are for low-mass satellites that joined later. While this points to outside-in quenching operating in these systems, the $\Delta\Sigma_{\mathrm{SFR}}$ profile of the population with $1.0 < z_j < 1.5$ (Figure 12) shows evidence of active star formation occurring at $\approx 1.25R_e$, although this population is highly variable.

The redshift at which a satellite joined its host serves as a statistical proxy for cumulative environmental interactions the satellite has experienced. In contrast, ΔM_{SFG} is a direct measurement of the net effect of these interactions on the total mass of available star forming gas. It is no surprise, then, that age_L profiles subdivided by $\Delta M_{\mathrm{SFG}}/M_*$ are clearly separated in age. Low-mass satellites with $\Delta M_{\mathrm{SFG}}/M_* > 0.25$ have a total median luminosity-weighted age of ≈ 370 Myr, while low-mass satellites with $\Delta M_{\mathrm{SFG}}/M_* < -0.25$ have a total median age_L of ≈ 6.7 Gyr and are completely quenched in the outskirts (Figure 14a)).

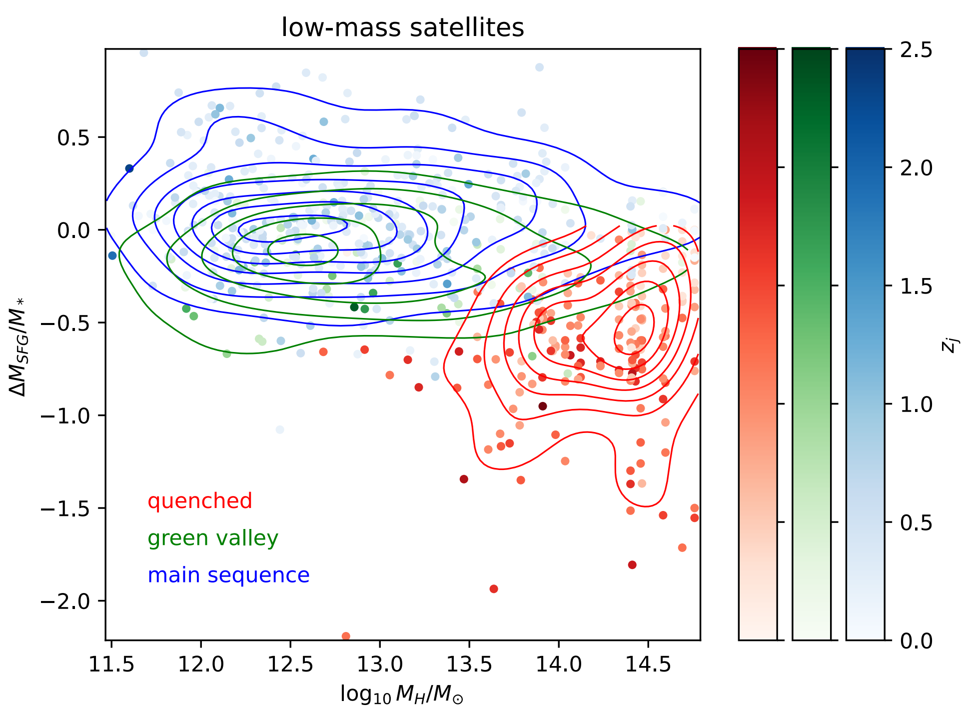

Figure 16. The relationship between halo mass and change in mass of star forming gas since joining, for main sequence (blue), green valley (green), and quenched (red) low-mass satellites. Density contours are drawn for the separate populations, and individual galaxies are plotted as points that are colored according to their star-formation type and joining redshift, z_j.

What drives the change in star-forming gas mass for low-mass TNG100 satellite galaxies? Of all the parameters explored in Appendix A, $\Delta M_{\mathrm{SFG}}/M_*$ is best correlated with z_j, although it is not a tight correlation. However, the redshift at which a satellite joined its host's halo is not indicative of the actual physical processes that are occurring.

In Appendix A, we show correlations with $\Delta M_{\rm SFG}/M_*$ for z_j, M_H, and δ_5, with satellites separated by mass and star formation type (Figure 19). In Figure 16, we show the most significant correlation for low-mass satellites: $\Delta M_{\rm SFG}/M_*$ and M_H. Most quenched, low-mass satellites joined high-mass halos relatively early and have lost significant amounts of gas by the present day. The quenched population has greater overlap with main-sequence and green valley galaxies in the $\Delta M_{\rm SFG}/M_* - \delta_5$ parameter space (see Figure 19 in Appendix A). Thus, we can infer that quenching of low-mass TNG100 satellite galaxies is driven more typically by environmental processes related to their hosts' halos, rather than galaxy-galaxy interactions that scale with δ_5. Host halos have a greater chance of removing gas from the satellites over longer timescales, driving the correlation of quenching with early z_j. In a study of SDSS-MaNGA satellites, Oyarzún et al. (2023) reached similar conclusions regarding the environmental quenching of observed low-mass satellites in high-mass halos over time.

It is important to note that this is a very general picture, and there are many exceptions, as can be seen in Figure 16. In some cases, TNG100 satellites that joined their hosts only recently can still lose large amounts of star-forming gas. In addition, there are satellites that joined their hosts in the distant past, but remain actively star forming at the present day, with some having even gained star-forming gas. We conclude that gas removal and quenching in low-mass satellites tends to be dominated by interactions with their hosts' halos and is dependent on the exact nature of the interactions that individual satellites experience. This interpretation is consistent with results from the FOGGIE simulations, which have shown that ram pressure stripping of satellites at $z = 2$ is stochastic and highly dependent on the paths of individual satellites through the circumgalactic medium (Simons et al. 2020). Additionally, using the cosmological hydrodynamic code Enzo (Tonnesen et al. 2007) to simulate a massive cluster, Tonnesen & Bryan (2008) found that the ram pressure force exerted on satellites at the same cluster-centric distance could vary by over an order of magnitude due to differences in local density and relative speed. Finding relatively high metallicities in rapidly quenched, low-mass satellite galaxies, the results of Corcho-Caballero et al. (2023) indicate that these systems are quenched following a starbursting period triggered by environmental interactions. Regardless of how it occurs, radial profiles of age$_L$ and $\Delta\Sigma_{\rm SFR}$ show that environmental quenching occurs from the outside-in in TNG100 galaxies, in agreement with observations, e.g., Finn et al. (2018), Lin et al. (2019), Bluck et al. (2020b), and Matharu et al. (2021).

Our conclusion that low-mass satellite quenching is more dependent on halo mass than it is on local galaxy density is in tension with the results of Bluck et al. (2020b). Using a random forest classification analysis, Bluck et al. (2020b) found that local galaxy overdensity was most predictive of quenched spaxels in low-mass satellite galaxies observed by MaNGA. Halo mass was the second most important environmental parameter, and distance to the host galaxy was found to be of little importance. We note, however, that measurements of M_H and δ_5 are much more challenging in observations than they are in simulations. In the case of Bluck et al. (2020b), the halo masses were derived from abundance matching techniques, which could result in a stronger correlation of M_H with δ_5 than is physical. However, this tension could also result from limitations in the simulation, for example the spatial resolution at which the gas physics is captured, particularly during mergers or other interactions (Sparre & Springel 2016). Further work in both observations and simulations would be necessary in order to determine whether the primary driver of low-mass satellite quenching is galaxy-galaxy interactions (correlated with δ_5) or galaxy-halo interactions (correlated with M_H). We remind readers that simulations are based on theoretical models, and may not represent reality.

6. SUMMARY

In this paper, we constructed radial profiles of age$_L$ and $\Delta\Sigma_{\rm SFR}$ for various populations of galaxies in the TNG100 simulation in order to investigate the degree to which the profiles are affected by intrinsic and environmental factors. We constructed these profiles separately for central and satellite galaxies with low- and high- masses ($M_* < 10^{10} M_\odot$ and $M_* > 10^{10.5} M_\odot$, respectively). Our main results for galaxies in the TNG100 simulation are as follows:

- The shapes and normalizations of averaged radial profiles of high-mass ($M_* > 10^{10.5} M_\odot$) galaxies (whether central or satellite) are strongly dependent on black hole mass (M_{BH}, Figures 1 and 2) and cumulative AGN feedback imparted on the galaxies ($\Sigma E_{\rm QM}$, Figures 3 and 4). The shapes of these profiles are consistent with inside-out quenching.

- High-mass galaxies in extreme environments (Figure 7: $M_H/M_\odot > 10^{13.5}$ for central galaxies and $M_H/M_\odot > 10^{14}$ for satellite galaxies and/or Figure 9: $\delta_5 > 10^{1.5}$) have age$_L$ profiles that become slightly positive at large radii. This indicates that galaxies in extreme environments can be quenched from both inside-out and outside-in.

- Population-averaged age$_L$ and $\Delta\Sigma_{\rm SFR}$ profiles of low-mass galaxies are similar across several magnitudes of black hole mass. This is also the case for low-mass central galaxies when binned by $\Sigma E_{\rm QM}$ (Figures 3 and 4). When low-mass satellites are binned by $\Sigma E_{\rm QM}$, age$_L$ normalization increases with increasing $\Sigma E_{\rm QM}$ and $\Delta\Sigma_{\rm SFR}$ decreases. The averaged age$_L$ profile for low-mass satellites with $10^{13} < \Sigma E_{\rm QM} < 10^{15}$ is flatter in the outskirts compared to the other low-mass satellite $\Sigma E_{\rm QM}$ populations, and the $\Delta\Sigma_{\rm SFR}$ profile of this population is consistent with outside-in quenching.

- The age$_L$ and $\Delta\Sigma_{\rm SFR}$ profiles of low-mass central galaxies are not strongly dependent on δ_5 or M_H (Figures 7-10). The only exceptions are central galaxies in very low-mass halos ($M_H/M_\odot < 10^{11}$), which are much older than low-mass centrals in higher mass halos. This is likely the result of overcooling because the TNG100 model only seeds a SMBH in a galaxy once the halo mass reaches a threshold of $M_H/M_\odot \approx 10^{10.87}$. Only low-mass satellites in extreme environments ($M_H/M_\odot > 10^{13.5}$ and/or $\delta_5 > 10^{1.5}$) have age$_L$ and $\Delta\Sigma_{\rm SFR}$ profiles that differ significantly from the other low-mass satellite populations.

- The time a satellite has spent within its host's halo, z_j, has a greater effect on age$_L$ and $\Delta\Sigma_{\rm SFR}$ profiles of low-mass satellites than it does for high-mass satellites (Figures 11 and 12). The normalization of age$_L$ for low-mass satellites increases with increasing time in the halo and quenched regions appear in the $\Delta\Sigma_{\rm SFR}$ profiles at $z_j > 1.0$.

- While z_j serves as an imperfect proxy for environmental effects a satellite encounters in a host's halo, $\Delta M_{\rm SFG}$ directly measures the change in star-forming gas that a satellite has experienced since joining. The change in star-forming gas preferentially affects the outskirts of both high- and low-mass galaxies. For low-mass satellite galaxies, the shapes and normalizations of age$_L$ and $\Delta\Sigma_{\rm SFR}$ profiles are highly dependent on $\Delta M_{\rm SFG}$.

- Quenched low-mass satellites are found almost entirely within high-mass halos ($M_H/M_\odot > 10^{13.5}$, Figure 15). Quenched low-mass satellites are most distinct as a population in M_H-$\Delta M_{\rm SFG}$ parameter space (Figure 16). We infer that quenching in low-mass TNG100 satellites occurs when interactions with massive host halos deplete these galaxies of star-forming gas. These interactions are more likely to occur, and remove more gas, with increasing time spent in the halo. However, z_j and $\Delta M_{\rm SFG}$ are only loosely correlated with each other (Figure 18). Thus, the efficiency with which environmental processes (e.g., ram pressure stripping and galaxy-galaxy interactions) remove the gas reservoir appears to be highly dependent on the nature of individual interactions.

In conclusion, we find that high-mass galaxies, both centrals and satellites, in the TNG100 simulation are quenched from the inside-out via AGN feedback energy, in agreement with expectations based on previous observational and theoretical studies of quenching. Quenching in low-mass TNG100 satellites appears to be driven by interactions with their hosts' hot gas halos. These low-mass quenched populations are not always reflected in the average radial profiles of different environmental populations; the parameters we have explored only capture the likelihood of interactions occurring, rather than the natures of the interactions. Environmental effects drive quenching from the outside-in, resulting in radial age$_L$ profiles that are positive in slope beyond $R \sim 1 - 1.25R_e$ and $\Delta\Sigma_{\rm SFR}$ profiles that are quenched at large radii. We have shown previously that the radial profiles of age$_L$ and $\Delta\Sigma_{\rm SFR}$ for TNG100 galaxies are generally in agreement with observations (McDonough et al. 2023). However, the results we report here should still be interpreted with the understanding that simulations are limited by resolution, size, and the physical models that are employed.

We thank the reviewer for providing detailed feedback on our work. We would like to acknowledge the work and documentation provided by the IllustrisTNG team that has made this paper possible. The IllustrisTNG simulations were undertaken with compute time awarded by the Gauss Centre for Supercomputing (GCS) under GCS Large-Scale Projects GCS-ILLU and GCS-DWAR on the GCS share of the supercomputer Hazel Hen at the High Performance Computing Center Stuttgart (HLRS), as well as on the machines of the Max Planck Computing and Data Facility (MPCDF) in Garching, Germany. The additional computational work done for this paper was performed on the Shared Computing Cluster which is administered by Boston University's Research Computing Services. This work was partially supported by NSF grant AST-2009397. BM acknowledges support by Northeastern University's Future Faculty Postdoctoral Fellowship Program. We also thank Dr. Paul Tol for providing an online resource for sequential color maps that are colorblind-friendly.

Software: astropy (Astropy Collaboration et al. 2013, 2018, 2022)

REFERENCES

Abraham, R. G., van den Bergh, S., & Nair, P. 2003, ApJ, 588, 218, doi: 10.1086/373919

Astropy Collaboration, Robitaille, T. P., Tollerud, E. J., et al. 2013, A&A, 558, A33, doi: 10.1051/0004-6361/201322068

Astropy Collaboration, Price-Whelan, A. M., Sipőcz, B. M., et al. 2018, AJ, 156, 123, doi: 10.3847/1538-3881/aabc4f

Astropy Collaboration, Price-Whelan, A. M., Lim, P. L., et al. 2022, apj, 935, 167, doi: 10.3847/1538-4357/ac7c74

Beifiori, A., Courteau, S., Corsini, E. M., & Zhu, Y. 2012, Monthly Notices of the Royal Astronomical Society, 419, 2497, doi: 10.1111/j.1365-2966.2011.19903.x

Bluck, A. F. L., Maiolino, R., Sánchez, S. F., et al. 2020a, MNRAS, 492, 96, doi: 10.1093/mnras/stz3264

Bluck, A. F. L., Mendel, J. T., Ellison, S. L., et al. 2014, MNRAS, 441, 599, doi: 10.1093/mnras/stu594

Bluck, A. F. L., Piotrowska, J. M., & Maiolino, R. 2023, ApJ, 944, 108, doi: 10.3847/1538-4357/acac7c

Bluck, A. F. L., Mendel, J. T., Ellison, S. L., et al. 2016, MNRAS, 462, 2559, doi: 10.1093/mnras/stw1665

Bluck, A. F. L., Maiolino, R., Piotrowska, J. M., et al. 2020b, Monthly Notices of the Royal Astronomical Society, 499, 230, doi: 10.1093/mnras/staa2806

Bundy, K., Bershady, M. A., Law, D. R., et al. 2015, ApJ, 798, 7, doi: 10.1088/0004-637X/798/1/7

Cano-Díaz, M., Sánchez, S. F., Zibetti, S., et al. 2016, ApJL, 821, L26, doi: 10.3847/2041-8205/821/2/L26

Colombo, D., Sanchez, S. F., Bolatto, A. D., et al. 2020, A&A, 644, A97, doi: 10.1051/0004-6361/202039005

Corcho-Caballero, P., Ascasibar, Y., Sánchez, S. F., & López-Sánchez, Á. R. 2023, MNRAS, 520, 193, doi: 10.1093/mnras/stad147

Donnari, M., Pillepich, A., Nelson, D., et al. 2019, Monthly Notices of the Royal Astronomical Society, 485, 4817, doi: 10.1093/mnras/stz712

Ellison, S. L., Sánchez, S. F., Ibarra-Medel, H., et al. 2018, MNRAS, 474, 2039, doi: 10.1093/mnras/stx2882

Finn, R. A., Desai, V., Rudnick, G., et al. 2018, ApJ, 862, 149, doi: 10.3847/1538-4357/aac32a

García-Benito, R., Zibetti, S., Sánchez, S. F., et al. 2015, A&A, 576, A135, doi: 10.1051/0004-6361/201425080

Genel, S., Nelson, D., Pillepich, A., et al. 2018, MNRAS, 474, 3976, doi: 10.1093/mnras/stx3078

González Delgado, R. M., Pérez, E., Cid Fernandes, R., et al. 2014, A&A, 562, A47, doi: 10.1051/0004-6361/201322011

González Delgado, R. M., Cid Fernandes, R., Pérez, E., et al. 2016, A&A, 590, A44, doi: 10.1051/0004-6361/201628174

Lin, L., Hsieh, B.-C., Pan, H.-A., et al. 2019, ApJ, 872, 50, doi: 10.3847/1538-4357/aafa84

Lotz, J. M., Primack, J., & Madau, P. 2004, AJ, 128, 163, doi: 10.1086/421849

Ma, W., Liu, K., Guo, H., et al. 2022, ApJ, 941, 205, doi: 10.3847/1538-4357/aca326

Marasco, A., Poggianti, B. M., Fritz, J., et al. 2023, Monthly Notices of the Royal Astronomical Society, 525, 5359, doi: 10.1093/mnras/stad2604

Marinacci, F., Vogelsberger, M., Pakmor, R., et al. 2018, MNRAS, 480, 5113, doi: 10.1093/mnras/sty2206

Martig, M., Bournaud, F., Teyssier, R., & Dekel, A. 2009, ApJ, 707, 250, doi: 10.1088/0004-637X/707/1/250

Matharu, J., Muzzin, A., Brammer, G. B., et al. 2021, ApJ, 923, 222, doi: 10.3847/1538-4357/ac26c3

McDonough, B., Curtis, O., & Brainerd, T. G. 2023, ApJ, 958, 19, doi: 10.3847/1538-4357/acfe0b

Naab, T., & Ostriker, J. P. 2017, ARA&A, 55, 59, doi: 10.1146/annurev-astro-081913-040019

Naiman, J. P., Pillepich, A., Springel, V., et al. 2018, MNRAS, 477, 1206, doi: 10.1093/mnras/sty618

Nelson, D., Pillepich, A., Genel, S., et al. 2015, Astronomy and Computing, 13, 12, doi: 10.1016/j.ascom.2015.09.003

Nelson, D., Pillepich, A., Springel, V., et al. 2018, MNRAS, 475, 624, doi: 10.1093/mnras/stx3040

Nelson, D., Springel, V., Pillepich, A., et al. 2019, Comput. Astrophys., 6, 2

Nelson, E. J., Tacchella, S., Diemer, B., et al. 2021, Monthly Notices of the Royal Astronomical Society, 508, 219, doi: 10.1093/mnras/stab2131

Oyarzún, G. A., Bundy, K., Westfall, K. B., et al. 2023, ApJ, 947, 13, doi: 10.3847/1538-4357/acbbca

Pan, H.-A., Lin, L., Ellison, S. L., et al. 2024, ApJ, 964, 120, doi: 10.3847/1538-4357/ad28c1

Peng, Y.-j., Lilly, S. J., Renzini, A., & Carollo, M. 2012, ApJ, 757, 4, doi: 10.1088/0004-637X/757/1/4

Peng, Y.-j., Lilly, S. J., Kovač, K., et al. 2010, ApJ, 721, 193, doi: 10.1088/0004-637X/721/1/193

Pillepich, A., Nelson, D., Hernquist, L., et al. 2018, MNRAS, 475, 648, doi: 10.1093/mnras/stx3112

Planck Collaboration. 2016, A&A, 594, A13

Reines, A. E., & Volonteri, M. 2015, ApJ, 813, 82, doi: 10.1088/0004-637X/813/2/82

Rodriguez-Gomez, V., Snyder, G. F., Lotz, J. M., et al. 2019, MNRAS, 483, 4140, doi: 10.1093/mnras/sty3345

Saglia, R. P., Opitsch, M., Erwin, P., et al. 2016, ApJ, 818, 47, doi: 10.3847/0004-637X/818/1/47

Sánchez, S. F. 2020, ARA&A, 58, 99, doi: 10.1146/annurev-astro-012120-013326

Sánchez, S. F., Walcher, C. J., Lopez-Cobá, C., et al. 2021, RMxAA, 57, 3, doi: 10.22201/ia.01851101p.2021.57.01.01

Sánchez, S. F., Rosales-Ortega, F. F., Jungwiert, B., et al. 2013, A&A, 554, A58, doi: 10.1051/0004-6361/201220669

Sarzi, M., Rix, H.-W., Shields, J. C., et al. 2005, ApJ, 628, 169, doi: 10.1086/428637

Sérsic, J. L. 1963, Boletin de la Asociacion Argentina de Astronomia La Plata Argentina, 6, 41

Silk, J., & Mamon, G. A. 2012, Research in Astronomy and Astrophysics, 12, 917, doi: 10.1088/1674-4527/12/8/004

Simons, R. C., Peeples, M. S., Tumlinson, J., et al. 2020, ApJ, 905, 167, doi: 10.3847/1538-4357/abc5b8

Snyder, G. F., Torrey, P., Lotz, J. M., et al. 2015, Monthly Notices of the Royal Astronomical Society, 454, 1886, doi: 10.1093/mnras/stv2078

Sparre, M., & Springel, V. 2016, MNRAS, 462, 2418, doi: 10.1093/mnras/stw1793

Spindler, A., Wake, D., Belfiore, F., et al. 2018, Monthly Notices of the Royal Astronomical Society, 476, 580, doi: 10.1093/mnras/sty247

Springel, V., Pakmor, R., Pillepich, A., et al. 2018, MNRAS, 475, 676, doi: 10.1093/mnras/stx3304

Steyrleithner, P., Hensler, G., & Boselli, A. 2020, MNRAS, 494, 1114, doi: 10.1093/mnras/staa775

Tonnesen, S., & Bryan, G. L. 2008, ApJL, 684, L9, doi: 10.1086/592066

Tonnesen, S., Bryan, G. L., & van Gorkom, J. H. 2007, ApJ, 671, 1434, doi: 10.1086/523034

Villanueva, V., Bolatto, A. D., Vogel, S. N., et al. 2024, ApJ, 962, 88, doi: 10.3847/1538-4357/ad1387

Vogelsberger, M., Genel, S., Springel, V., et al. 2014, Nature, 509, 177, doi: 10.1038/nature13316

Wechsler, R. H., & Tinker, J. L. 2018, ARA&A, 56, 435, doi: 10.1146/annurev-astro-081817-051756

Weinberger, R., Springel, V., Hernquist, L., et al. 2017, MNRAS, 465, 3291, doi: 10.1093/mnras/stw2944

Weinberger, R., Springel, V., Pakmor, R., et al. 2018, MNRAS, 479, 4056, doi: 10.1093/mnras/sty1733

Wilkinson, A., Almaini, O., Wild, V., et al. 2021, Monthly Notices of the Royal Astronomical Society, 504, 4533, doi: 10.1093/mnras/stab965

Woo, J., Dekel, A., Faber, S. M., & Koo, D. C. 2015, MNRAS, 448, 237, doi: 10.1093/mnras/stu2755

Wuyts, S., Förster Schreiber, N. M., Nelson, E. J., et al. 2013, ApJ, 779, 135, doi: 10.1088/0004-637X/779/2/135

Zheng, Z., Wang, H., Ge, J., et al. 2017, MNRAS, 465, 4572, doi: 10.1093/mnras/stw3030

APPENDIX

A. INTER-CORRELATION OF PARAMETERS

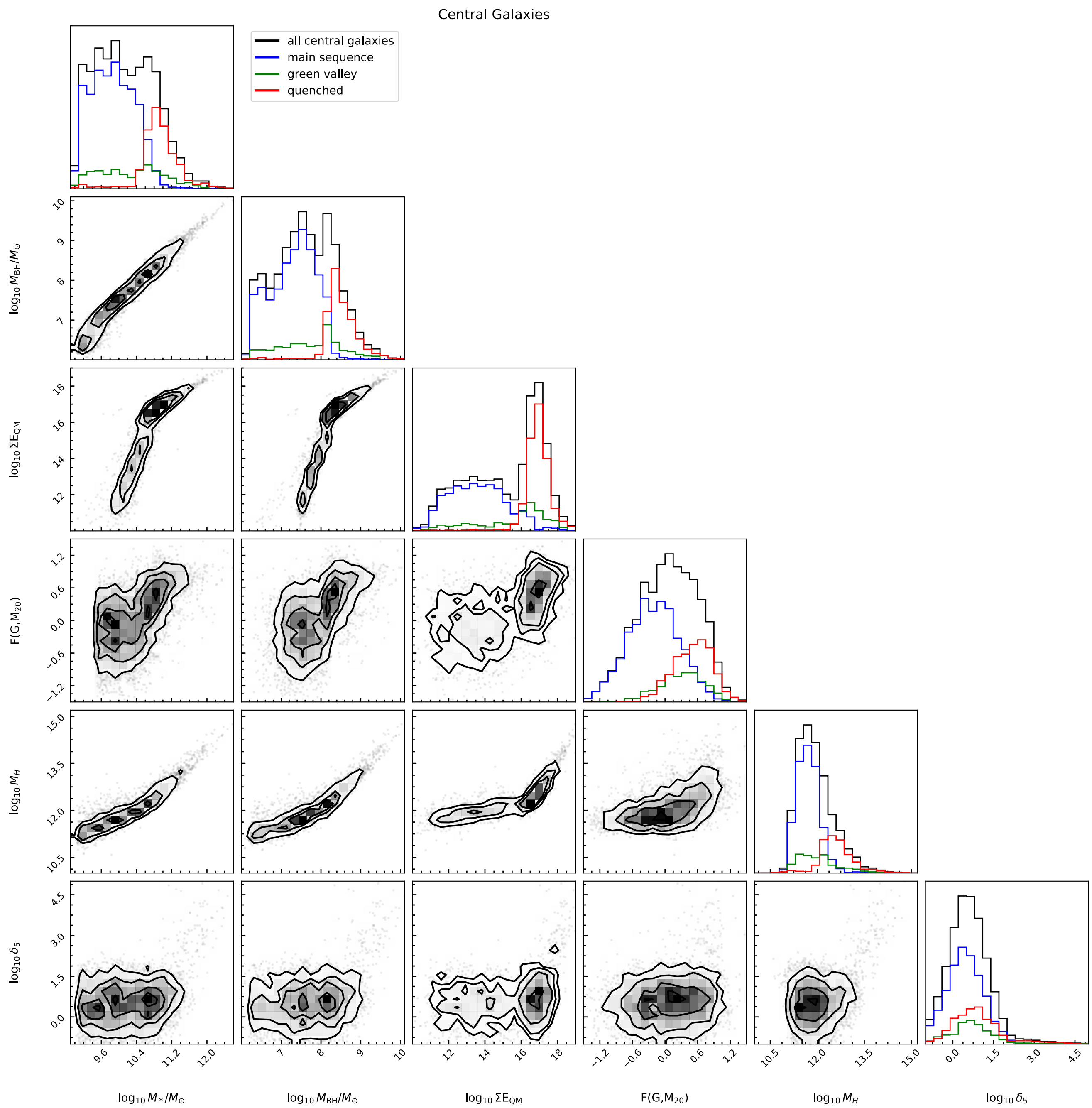

Figure 17. Corner plot illustrating correlations among the parameters explored in this paper, for central galaxies only. The diagonal displays the total distribution of each parameter (black), and the distribution separated by galaxy star-formation type: main sequence (blue), green valley (green), and quenched (red). Off-diagonal plots are two-dimensional histograms revealing relationships between two parameters. Contours are drawn at (0.5, 1, 1.5, 2)-sigma levels.

Galaxy evolution is a complex process that is by no means fully understood at this time. Adding to the inherent complexity of the galaxy evolution process is that parameters that describe properties of galaxies are often correlated, either through causation or co-evolution. Because of this, it is important to understand how the parameters we have explored in this paper are related to one another. In Figures 17 and 18, we present corner plots showing the relationships between the parameters we explored for central and satellite galaxies, respectively. On the diagonals, the one-dimensional distribution of each parameter is shown for all galaxies (black), and separately for galaxies based on their star-formation activity. Adopting the definitions from McDonough et al. (2023), we show the distributions for galaxies that are classified as quenched (red), green valley (green), or on the main sequence (blue).

Figure 17 shows the tight linear correlation between galaxy stellar mass and black hole mass, $M_* - M_{BH}$, for TNG100 central galaxies. Stellar mass is also correlated with total cumulative AGN energy imparted in the quasar mode, total halo mass, and, to a lesser extent, the bulge statistic. The existence of these correlations is well-documented in the literature (e.g., Beifiori et al. 2012; Reines & Volonteri 2015; Wechsler & Tinker 2018). On average, more massive TNG100 galaxies have more massive black holes, more massive halos, and more bulge-like morphologies. The total energy imparted by a SMBH is not directly observable, but it is expected to correlate well with black hole mass, as the imparted energy is related to the accretion rate. More massive galaxies are also more likely to be quenched.

On the diagonal in Figure 17, the distributions of quenched and main sequence central galaxies are distinct for all parameters related to stellar mass. At higher stellar masses, more galaxies are quenched. This phenomenon is thought to be driven by the central SMBH, and is often referred to as 'mass quenching' (Peng et al. 2010). The distribution is especially bimodal for cumulative energy injected, where quenched central galaxies lie almost entirely in the range of $\Sigma E_{\rm QM}$=$10^{16} - 10^{19}$. This provides further evidence that mass quenching is driven by the energy imparted by the SMBH.

Local galaxy overdensity is not correlated with stellar mass or other parameters, except at the highest galaxy masses. The most massive central galaxies will only exist in dense cluster centers, where they can accumulate stellar mass through accretion.

In Figure 18, we present the correlations between parameters for satellite galaxies. For parameters that are also measured in central galaxies, the plotted ranges are identical to 17. For satellite galaxies, we also include the $z_{\rm j}$ and $\Delta M_{\rm SFG}$ parameters. As for the central galaxies, there is a correlation between stellar mass and black hole properties (mass and energy injected), as well as a loose $M_* - F(G, M_{20})$ correlation. Here, halo mass is no longer correlated with stellar mass, since satellites reside within the larger halo of their central host galaxy. However, halo mass is correlated with δ_5. The redshift at which a satellite joined its host, z_j, and the change in star-forming gas, $\Delta M_{\rm SFG}$, are not

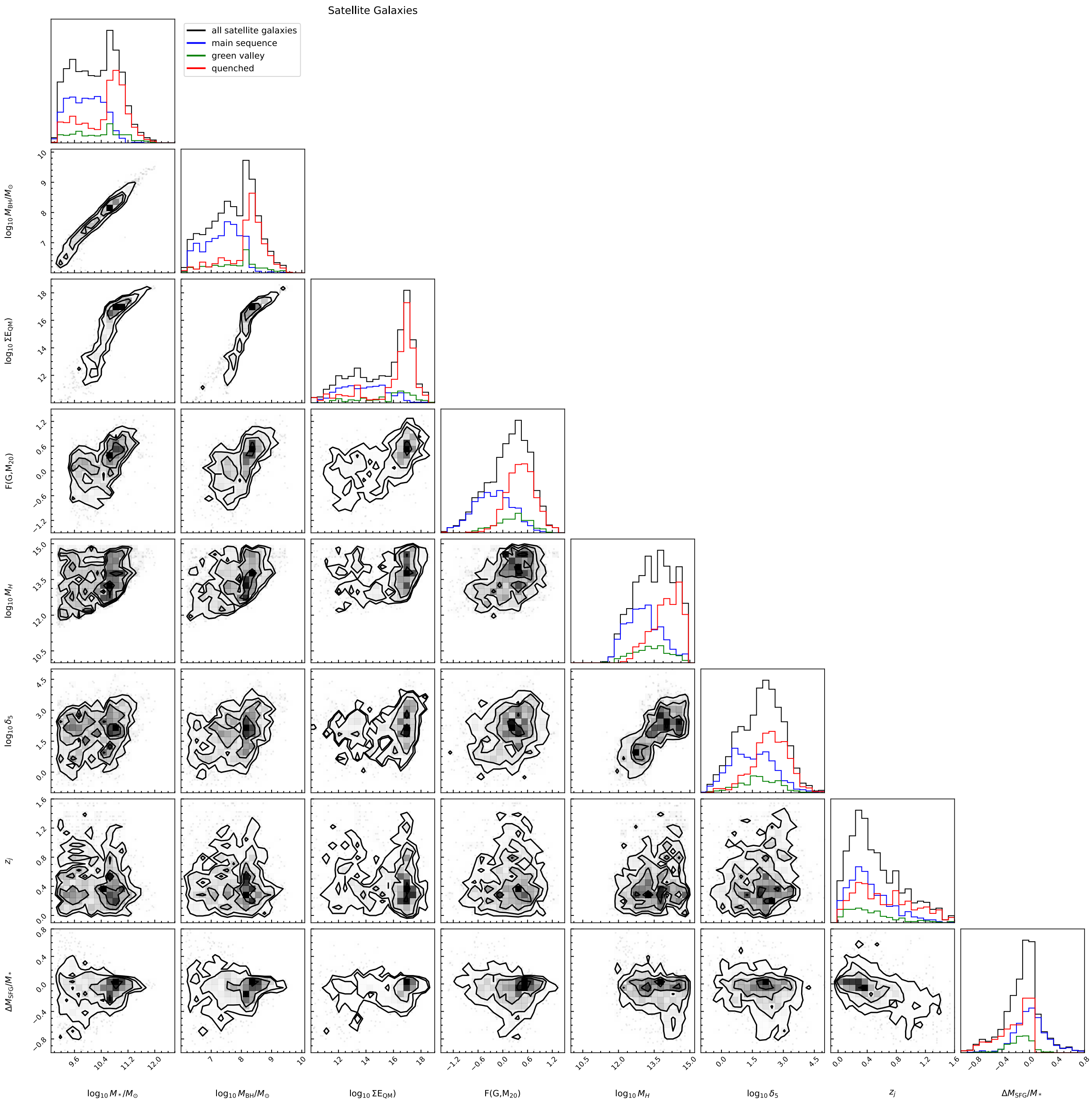

Figure 18. Corner plot illustrating correlations among the parameters explored in this paper, for satellite galaxies only. Formatting, including parameter ranges, is identical to Figure 17, with the addition of two parameters not computed for central galaxies: z_j and $\Delta M_{\rm SFG}$.

well correlated with any of the other parameters and are only slightly correlated with one another. The most negative values of $\Delta M_{\rm SFG}$ only occur at the highest halo masses.

Differences between the one-dimensional histograms in Figures 17 and 18 are especially illuminating. While only $\approx 6\%$ of quenched TNG100 central galaxies have $M_*/M_\odot < 10^{10.4}$, just over 50% of quenched TNG100 satellites fall

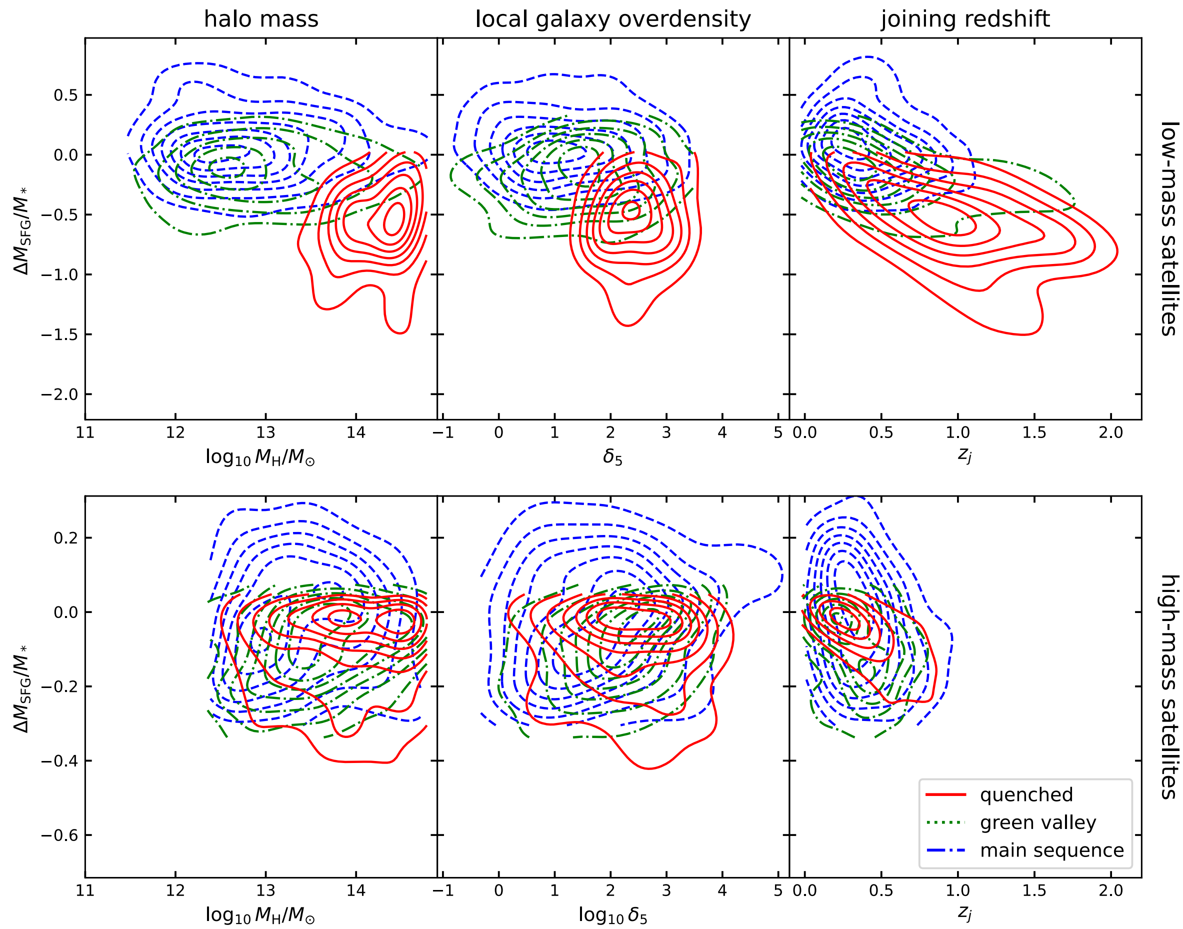

Figure 19. Correlation between $\Delta M_{\rm SFG}$ and environmental parameters for low-mass (top) and high-mass (bottom) satellite galaxies: halo mass (left), local galaxy overdensity (middle), and joining redshift (right). Density contours for the main sequence (blue), green valley (green), and quenched (red) populations are shown. Note that the ordinate limits differ between rows.

within this mass regime. The distributions of M_*, M_{BH}, and $\Sigma E_{\rm QM}$ for quenched satellite galaxies appear similar to the distributions of those parameters for quenched central galaxies, with an additional component at low values. This indicates that, while satellite galaxies will undergo mass quenching at high stellar masses, an additional quenching pathway is available for satellite galaxies.

This additional pathway allows for the quenching of low-mass satellite galaxies for which AGN feedback is weak or non-existent, and is most likely related to environmental processes. Quenched satellite galaxies are more likely to reside in more massive halos and in more dense areas, as shown in the distributions of M_H and δ_5 in Figure 18. The net effect of environmental processes is on the availability of star-forming gas.

The bottom right panel in Figure 18 shows the distribution of $\Delta M_{\rm SFG}$. When $\Delta M_{\rm SFG}$ is positive, star-forming gas has been added to the galaxy, likely through compression shocks or possibly accretion, resulting in main sequence galaxies at $z = 0$. In contrast, all quenched galaxies have values of $\Delta M_{\rm SFG}$that are zero or negative, indicating that these systems entered their hosts' halos as objects that were already quenched, or they were quenched as the halo stripped them of their star-forming gas.

As quenching occurs differently in galaxies of different masses, we further explore the correlation between $\Delta M_{\rm SFG}$ and M_H (left), δ_5 (center), and z_j (right) in Figure 19 for low- and high- mass satellites separately. From this figure, it is clear that the quenched (red) population of high-mass satellites (bottom row) differs very little from the main sequence (blue) or green valley (green) high-mass satellite populations in these parameter spaces. This is in contrast to the population of quenched low-mass satellites (top row). This indicates that quenching in high-mass satellite galaxies is not driven by environmental factors that remove star-forming gas, but it is the dominanat mechanism for quenching of low-mass satellites. A likely explanation for this phenomenon is that the greater gravitational potential of high-mass satellite galaxies better enables these systems to retain their gas reservoir during environmental interactions. The quenching in high-mass satellites is then primarily driven by AGN feedback energy, which introduces turbulence, reducing star formation efficiency.

Quenched, low-mass satellite galaxies form the most distinct population in $M_H - \Delta M_{\rm SFG}$ parameter space in Figure 19. Galaxy-galaxy interactions that scale with local galaxy overdensity could also drive star-forming gas loss, although it is correlated with halo mass (Figure 18). Low-mass satellites with high z_j are much more likely to be in the quenched or green valley populations, and z_j is loosely correlated with $\Delta M_{\rm SFG}$ loss.

B. SUMMARY OF GRADIENTS AND GLOBAL AVERAGES

In this appendix, we include figures that summarize the gradients reported in the legends of Figures 1 - 14 and the overall normalization of the profiles. For the normalization of age$_L$, we take the luminosity-weighted age of all stellar particles that are bound to the galaxy. For the normalization of $\Delta\Sigma_{\rm SFR}$, we report ΔSFR, the logarithmic distance from the star-forming main sequence line reported in McDonough et al. (2023). Figures 20 - 26 each summarize the results from one of the explored parameters: $M_{\rm BH}$, $\Sigma E_{\rm QM}$, $F(G, M_{20})$, $M_{\rm H}$, δ_5, z_j, and $\Delta M_{\rm SFG}$. The x-axes are the bins used in Figures 1 - 14, and points within those bins are arbitrarily offset for visibility. Low-mass galaxies are given in blue and high-mass galaxies are given in magenta. Central galaxies are shown as squares and satellite galaxies are shown as circles. From top to bottom, the panels are the median global age$_L$ for the population with errors given by the standard deviation, the age$_L$ gradient for the population with errors given by the fit, the median ΔSFR for the population with errors given by the standard deviation, and the gradient of $\Delta\Sigma_{\rm SFR}$ with errors given by the fit.

These figures do not capture the full variation in the shape of the radial profiles, but provide an overview of our results. The gradients reported are only measured from the center to $1R_e$, and therefore do not capture differences in the outer regions or between the disk and bulge regions.

C. MASS-DEPENDENCY OF NORMALIZATIONS

In this article, we have divided our sample into high- and low- mass galaxies ($M_* > 10^{10.5} M_\odot$ and $M_* < 10^{10} M_\odot$, respectively). However, the shape and normalization of age$_L$ and $\Delta\Sigma_{\rm SFR}$ profiles are mass-dependent (e.g., Figures 4 and 5 in McDonough et al. 2023). Many of the parameters we have explored in §3 and §4 are intrinsically related to stellar mass, which may modulate the effect. In this appendix, we present figures that explore how the cumulative age$_L$ and the logarithmic offset from the global star-forming main sequence (ΔSFR) for galaxies in our sample depend on stellar mass and the explored parameters. In Figures 27 - 31, we plot M_* against total age$_L$ (top rows) and ΔSFR (bottom rows) for central galaxies (left panels) and satellites (right panels). Points are colored by the value of the explored parameters for each galaxy. Figures 32 and 33 are identical in formatting, but only include a single column for satellite galaxies. While we use a similar color scheme, the point colors do not necessarily correspond to the colors of profiles in Figures 1 - 14. In Figures 29 and 33, we use a different color scheme that diverges at $F(G, M_{20})$= 0 and $\Delta M_{\rm SFG}$= 0 to emphasize the difference between galaxies with and without bulges and satellites that have lost and gained star-forming gas. We remind readers that low-levels of SFR in the simulation are not resolved, but are here artificially set to $sSFR = 10^{-12}{\rm yr}^{-1}$ with some scatter, which results in the linear trend appearing in some panels at $\Delta{\rm SFR} \sim -2$. We do not include figures that explore the mass-dependency of profile gradients because the profiles of individual galaxies are too noisy to obtain good estimates of the slopes, especially at lower masses where there are less stellar particles.

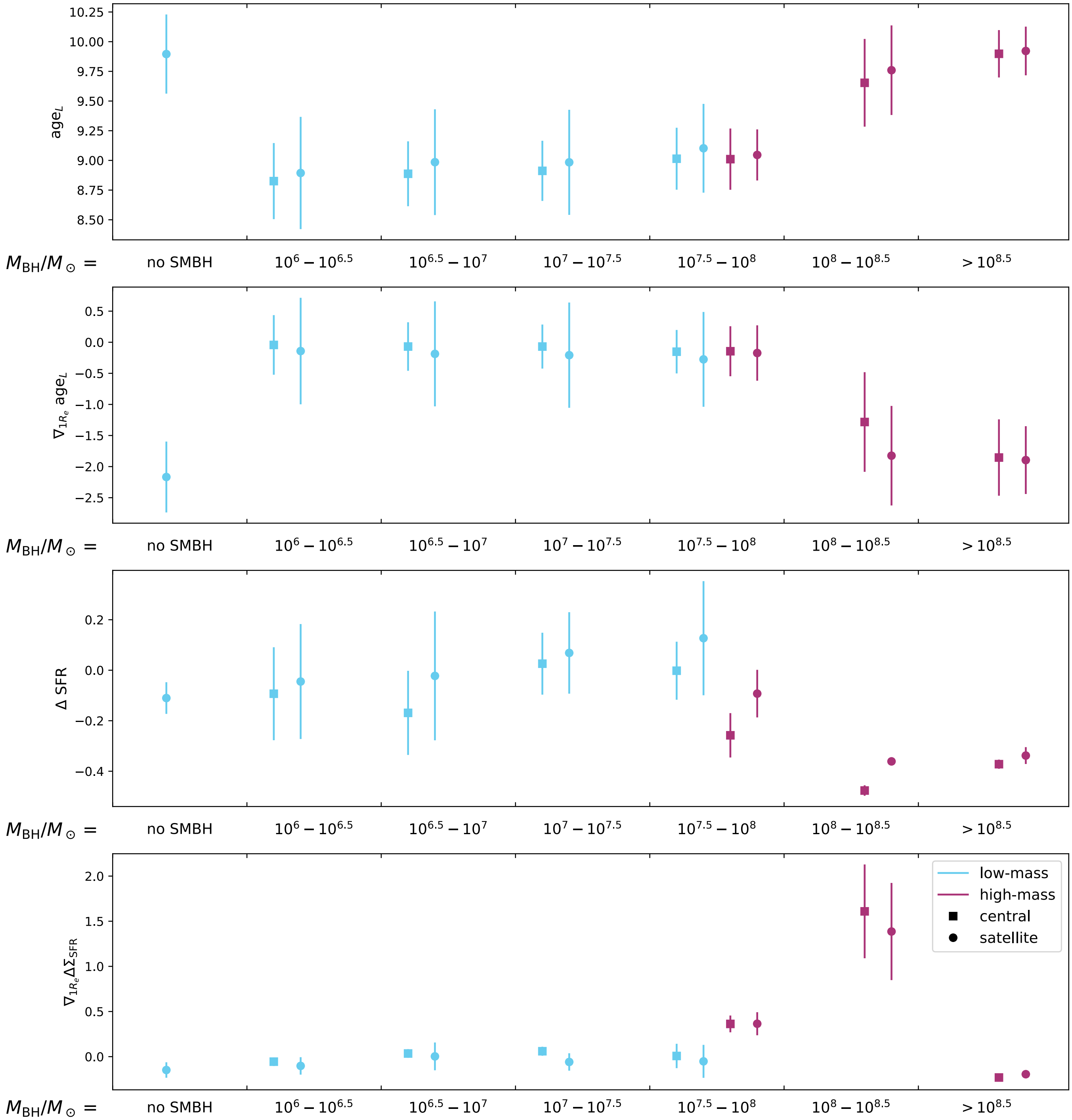

Figure 20. A summary of the median age$_L$ and SFR, as well as the gradients measured for populations of TNG100 galaxies whose radial profiles are shown in Figures 1 and 2. From top to bottom, the panels are the median global age$_L$ of each population subset, the age$_L$ gradient reported in the legend of Figure 1, the median offset from the global star-forming main sequence (ΔSFR), and the $\Delta\Sigma_{\rm SFR}$ gradients reported in the legend of Figure 2. The galaxy populations are divided into bins of $M_{\rm BH}/M_\odot$, which are given by the x-axis. Galaxies in these bins are further divided into high- and low- mass (magenta and blue, respectively) and classification as central or satellite galaxies (square and circle, respectively). Points within each bin are arbitrarily offset for visibility.

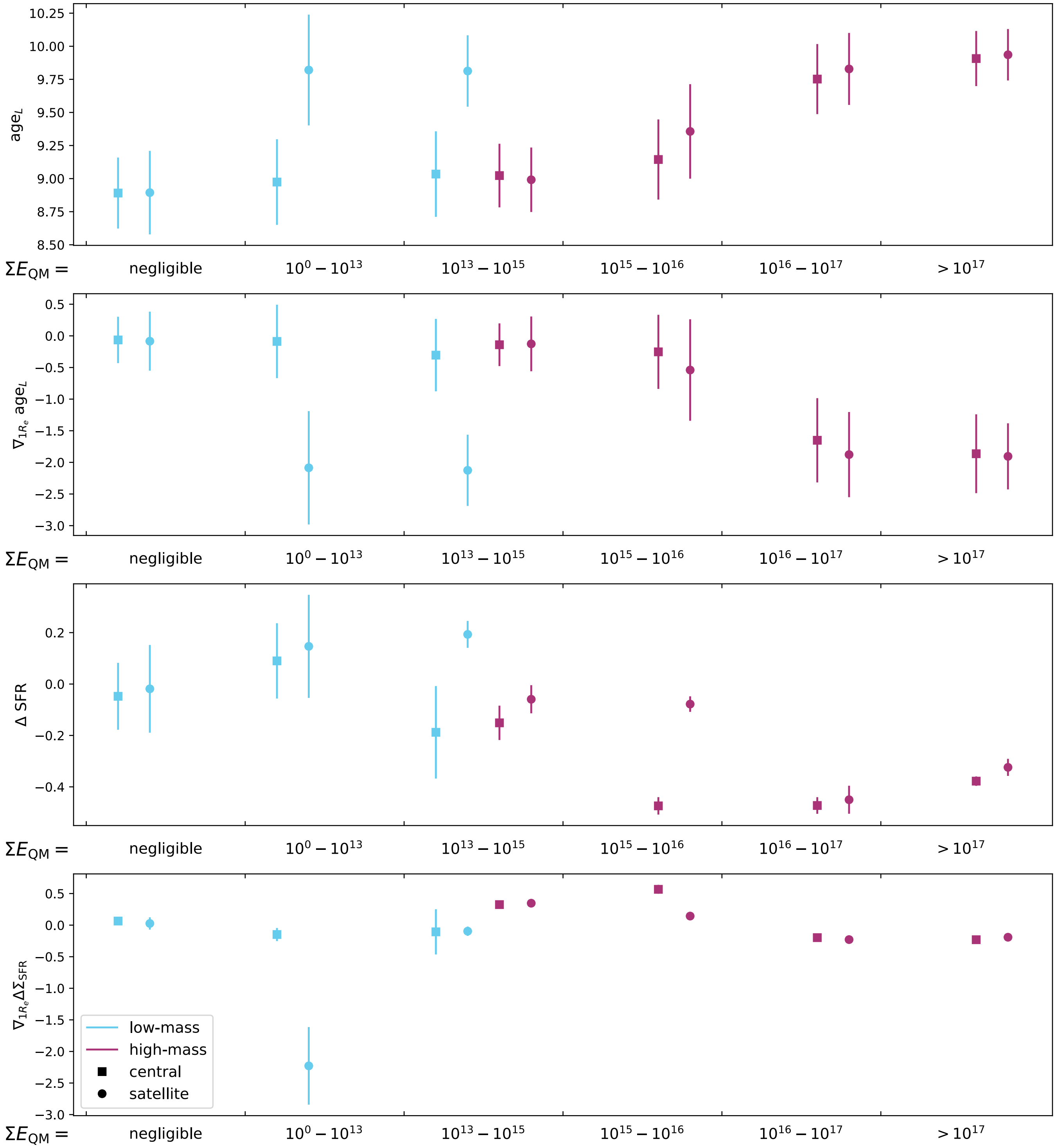

Figure 21. Formatting is identical to Figure 20, except the figure summarizes results from the $\Sigma E_{\rm QM}$ parameter shown in Figures 3 and 4.

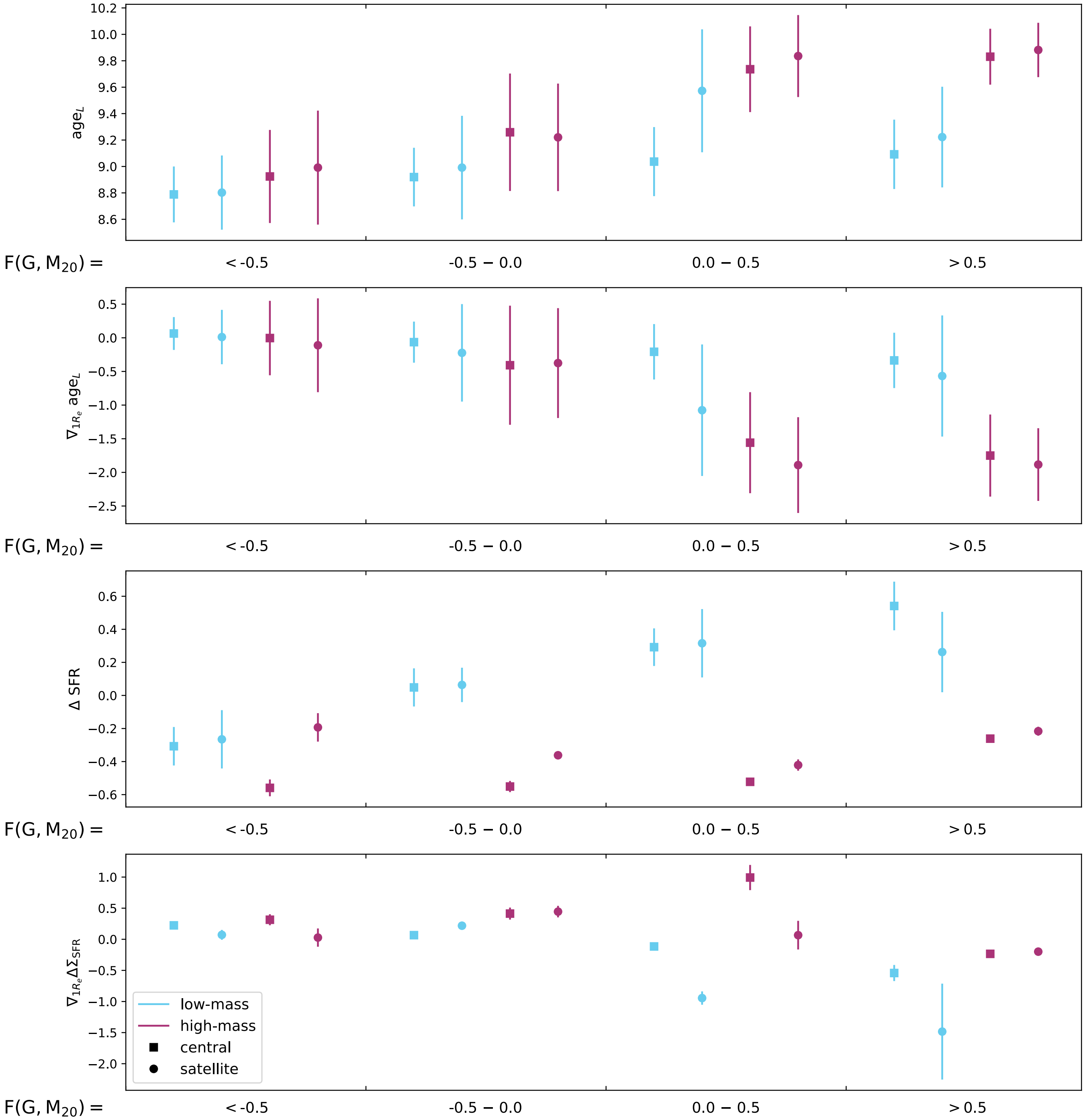

Figure 22. Formatting is identical to Figure 20, except the figure summarizes results from the $F(G, M_{20})$ parameter shown in Figures 5 and 6.

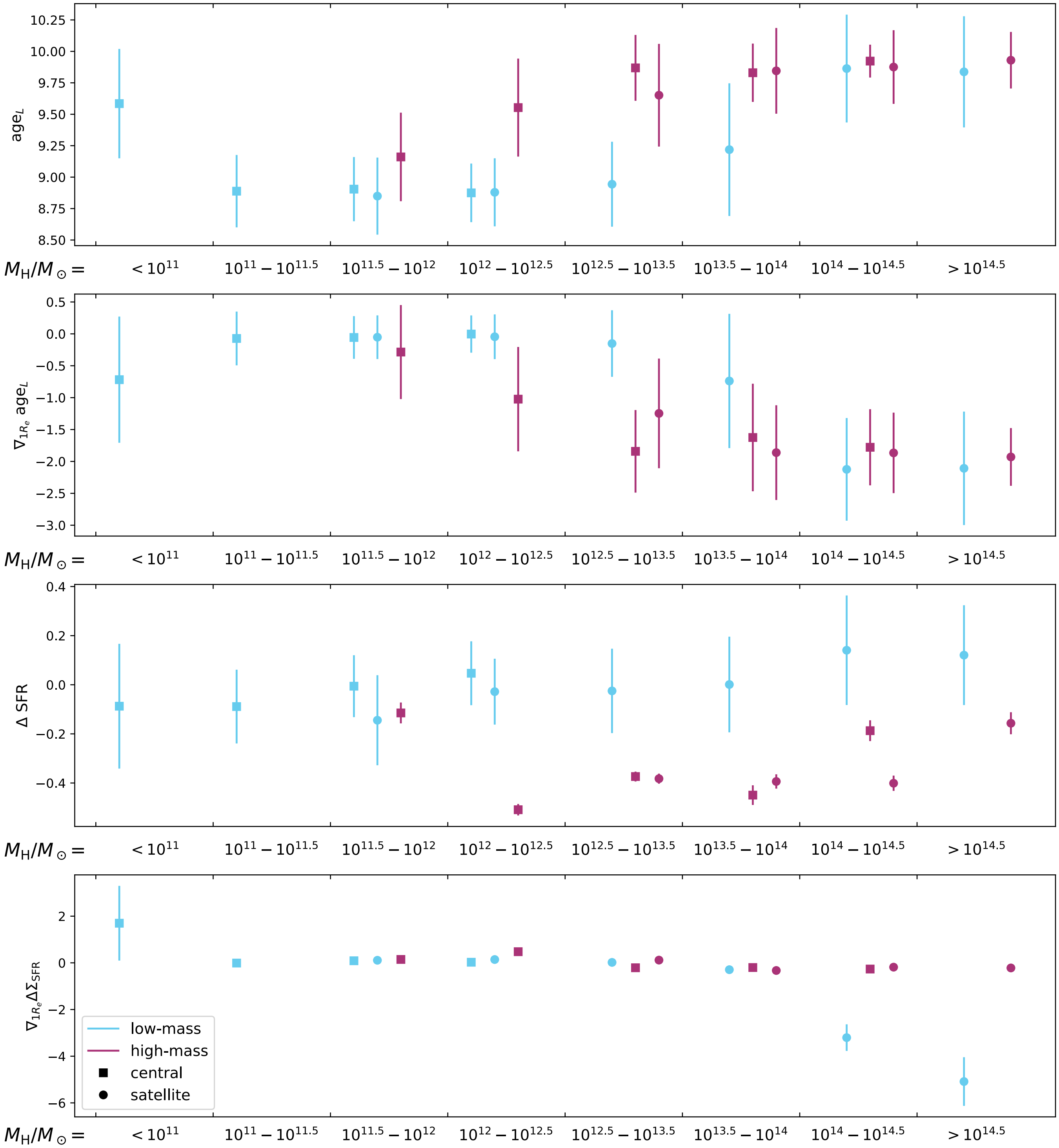

Figure 23. Formatting is identical to Figure 20, except the figure summarizes results for populations divided by $M_{\rm H}$ shown in Figures 7 and 8.

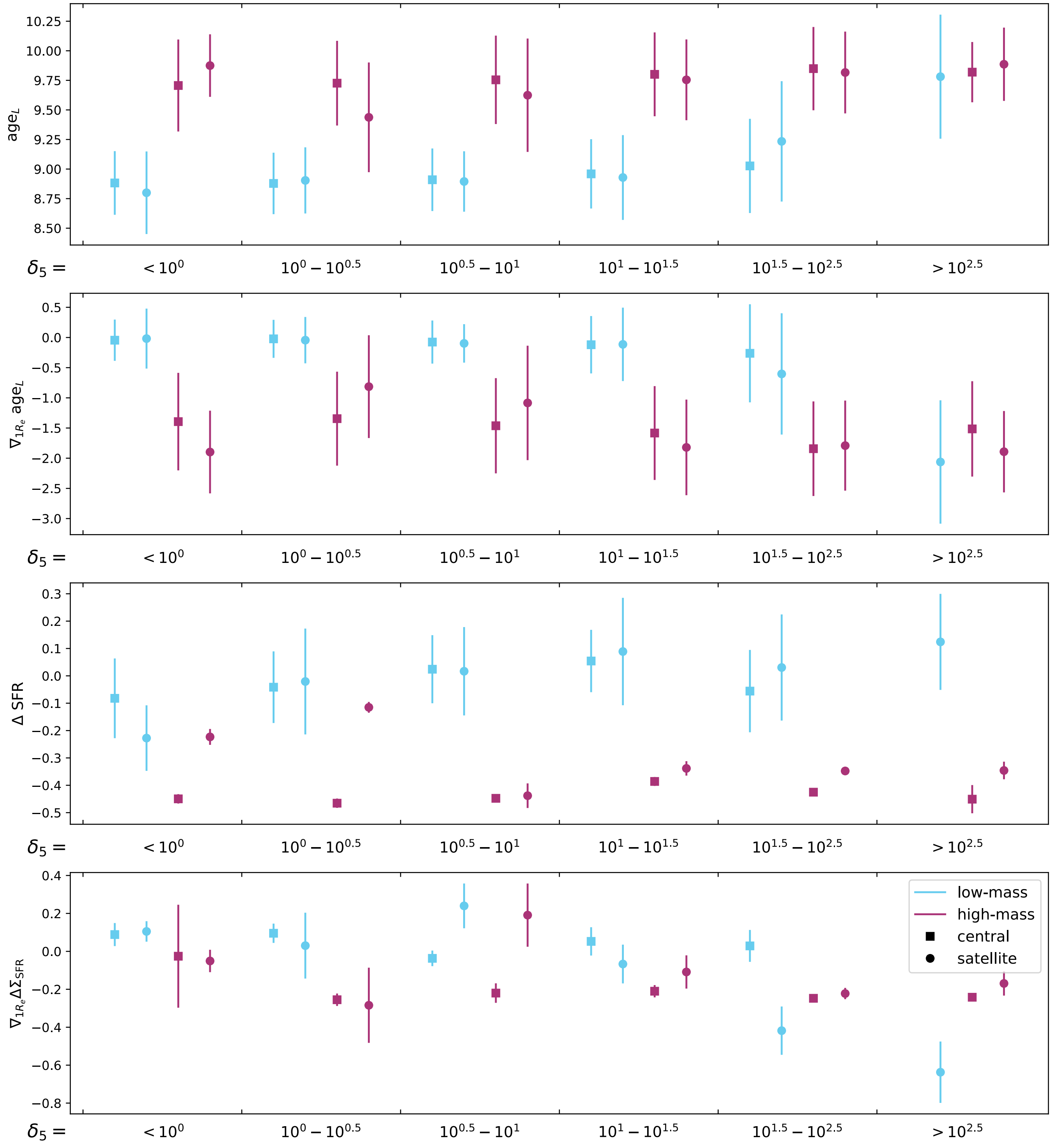

Figure 24. Formatting is identical to Figure 20, except the figure summarizes results for populations divided by δ_5 shown in Figures 9 and 10.

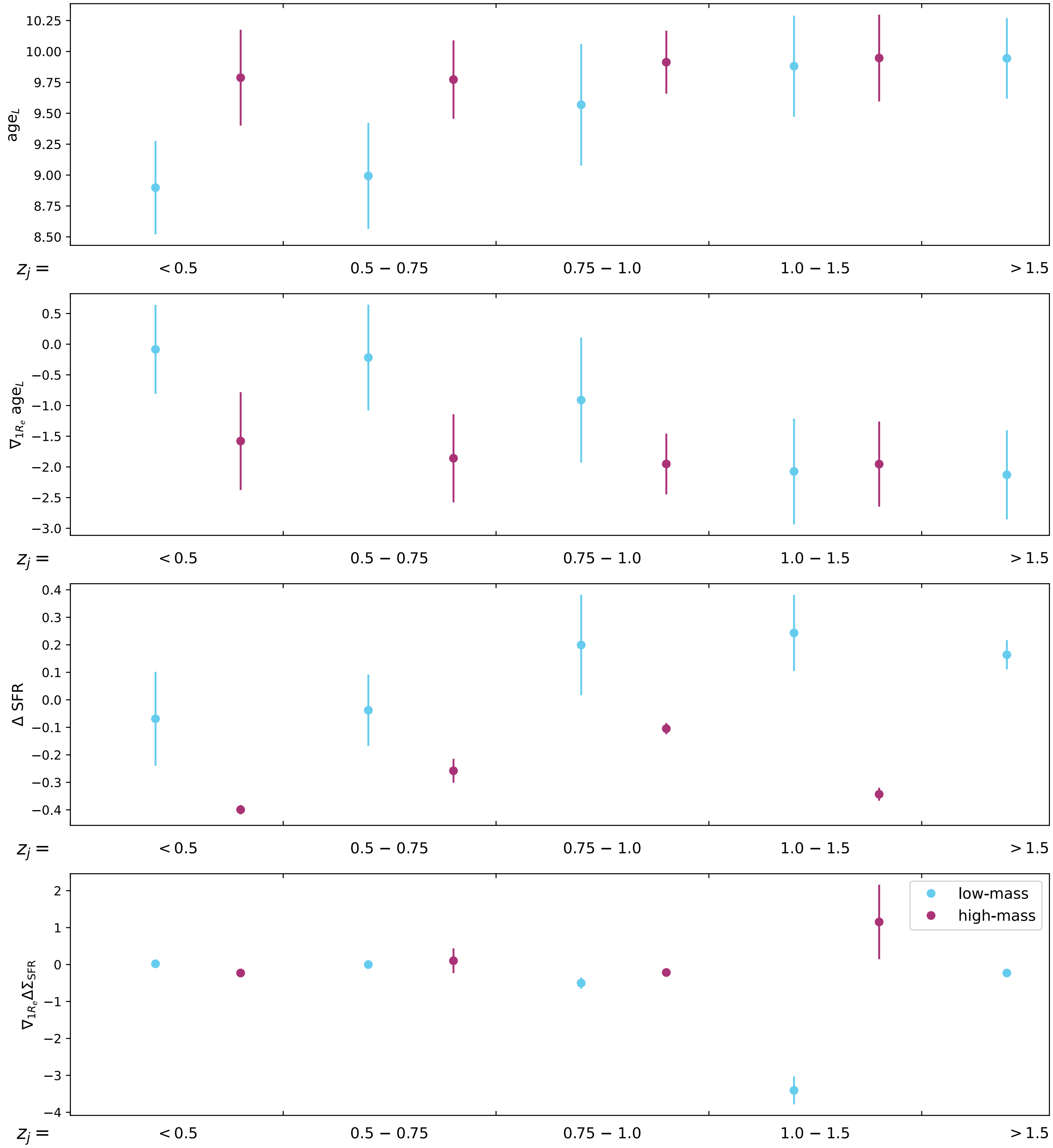

Figure 25. Formatting is identical to Figure 20, except the figure summarizes results for populations divided by z_j shown in Figures 11 and 12.

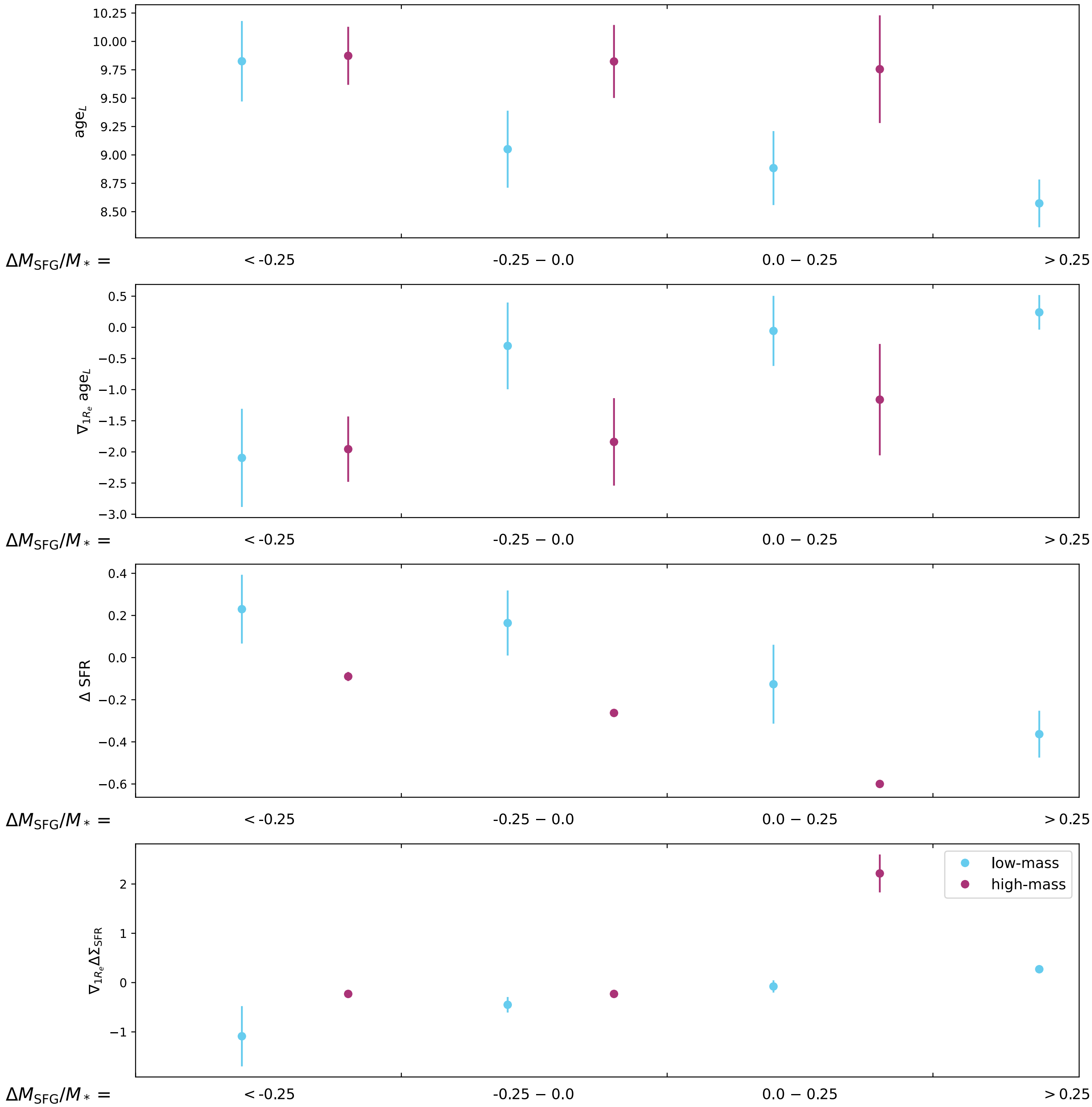

Figure 26. Formatting is identical to Figure 20, except the figure summarizes results for populations divided by $\Delta M_{\rm SFG}$ shown in Figures 13 and 14.

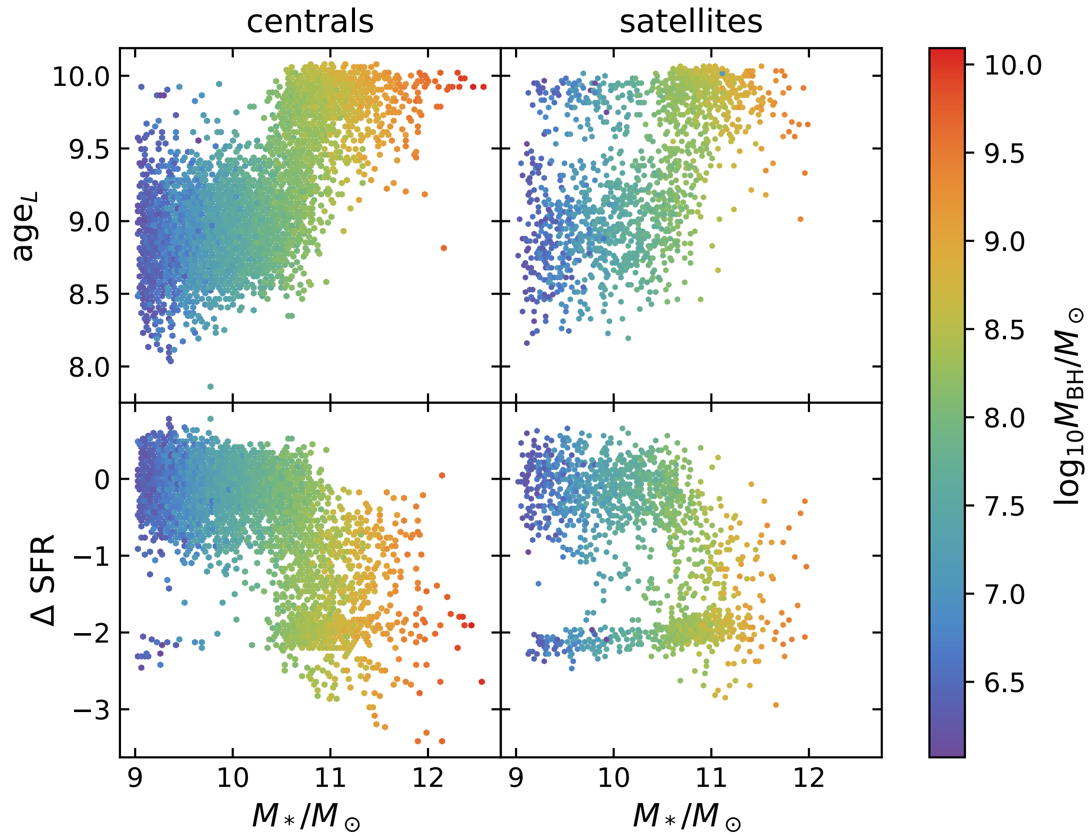

Figure 27. The total age$_L$ for a galaxy and the galaxy's logarithmic offset from the star-forming main sequence (ΔSFR) is plotted against stellar mass in the top and bottom panels, respectively. Central and satellite galaxies are plotted separately in the left and right columns, respectively. Points are colored according to the SMBH mass, $M_{\rm BH}$.

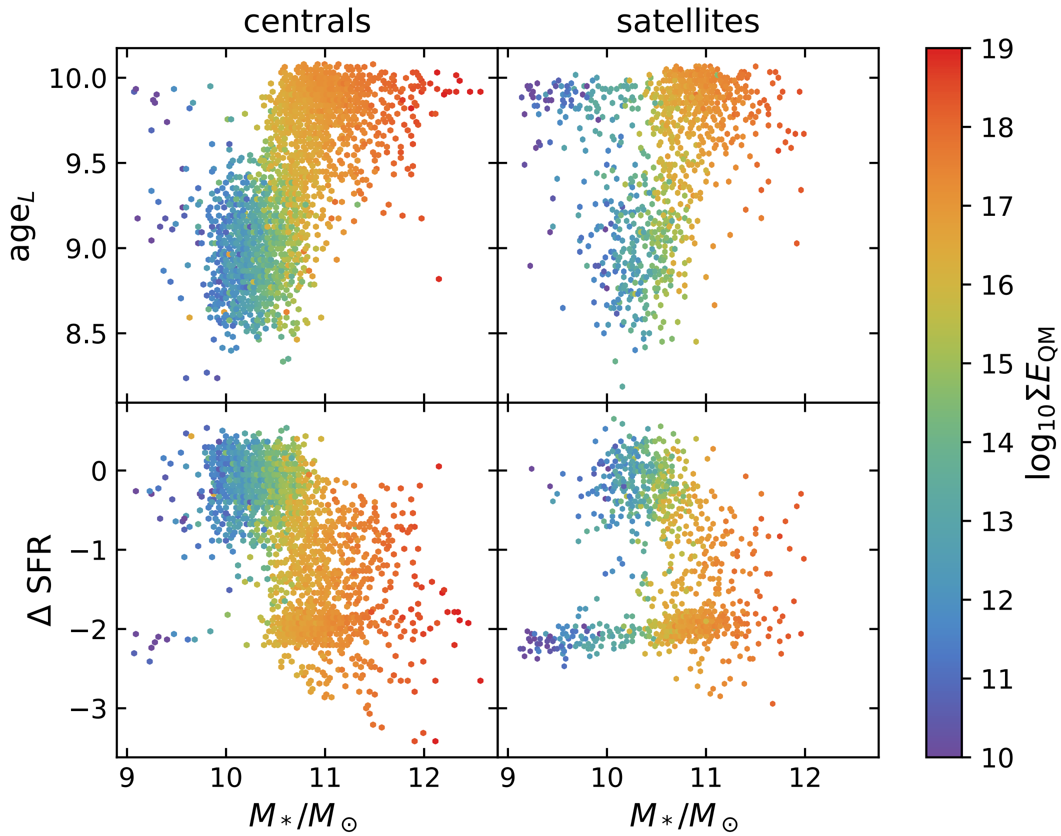

Figure 28. Formatting is identical to Figure 27, except points are colored by $\Sigma E_{\rm QM}$.

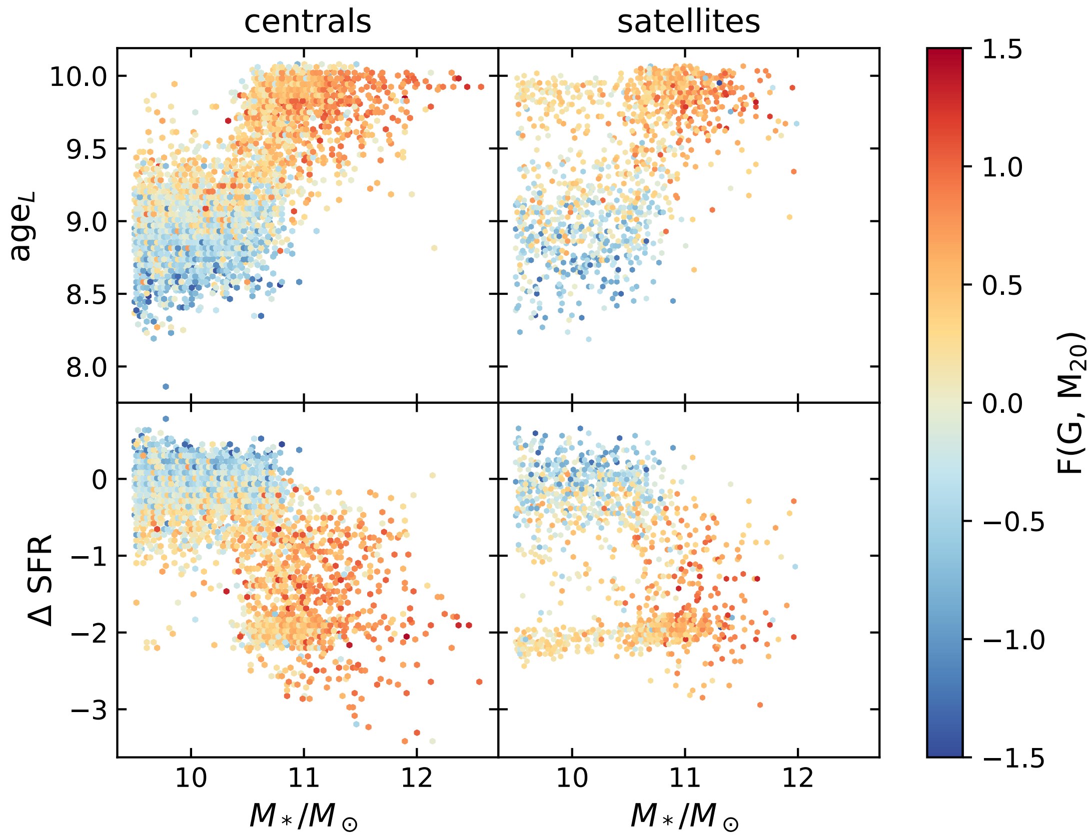

Figure 29. Formatting is identical to Figure 27, except points are colored by $F(G, M_{20})$.

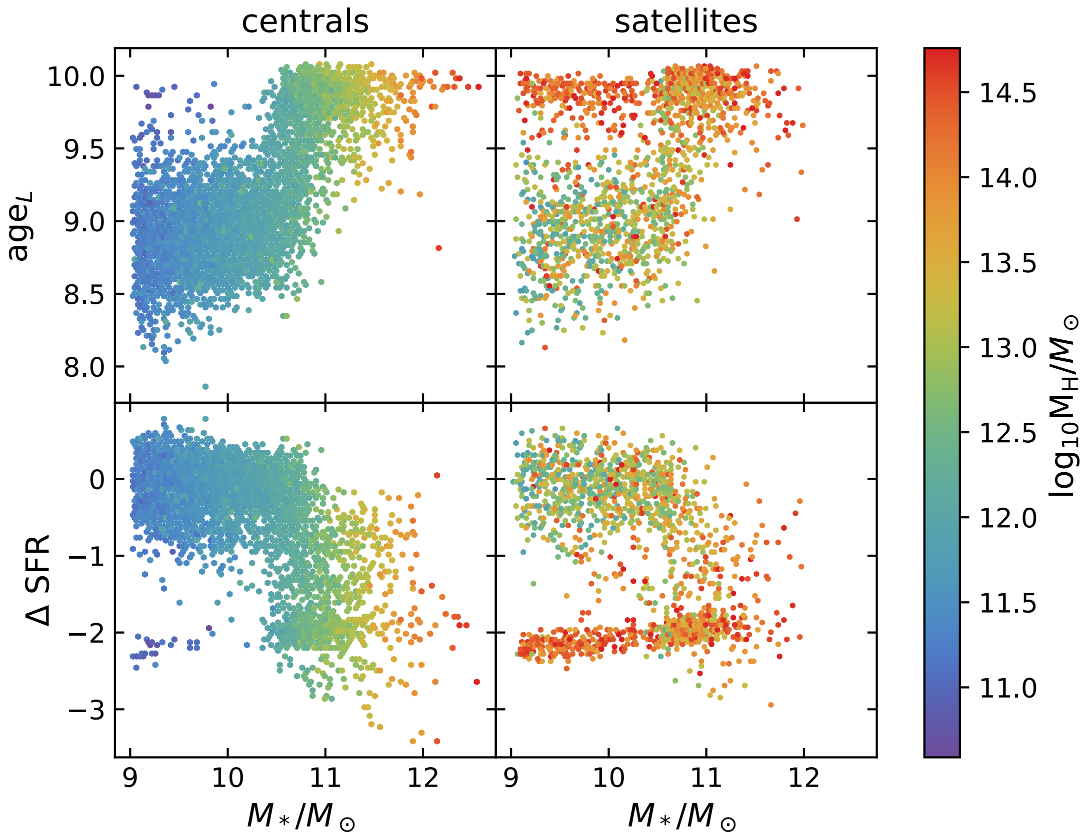

Figure 30. Formatting is identical to Figure 27, except points are colored by $M_{\rm H}$.

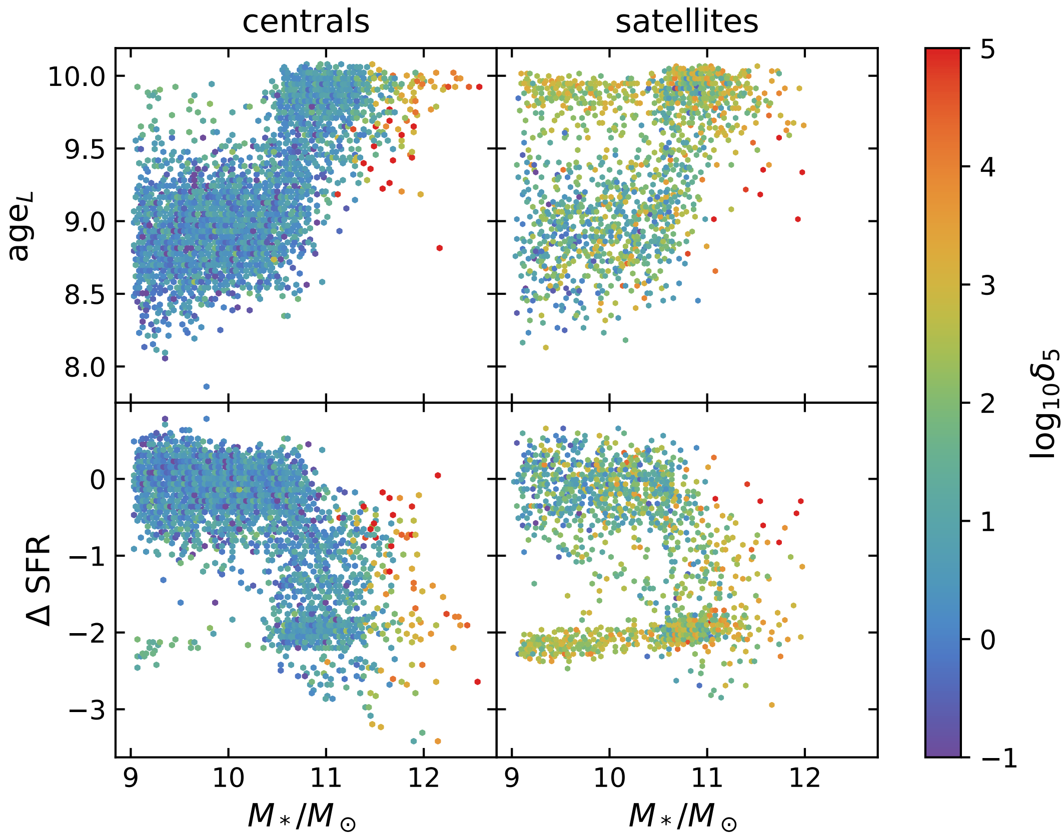

Figure 31. Formatting is identical to Figure 27, except points are colored by δ_5.

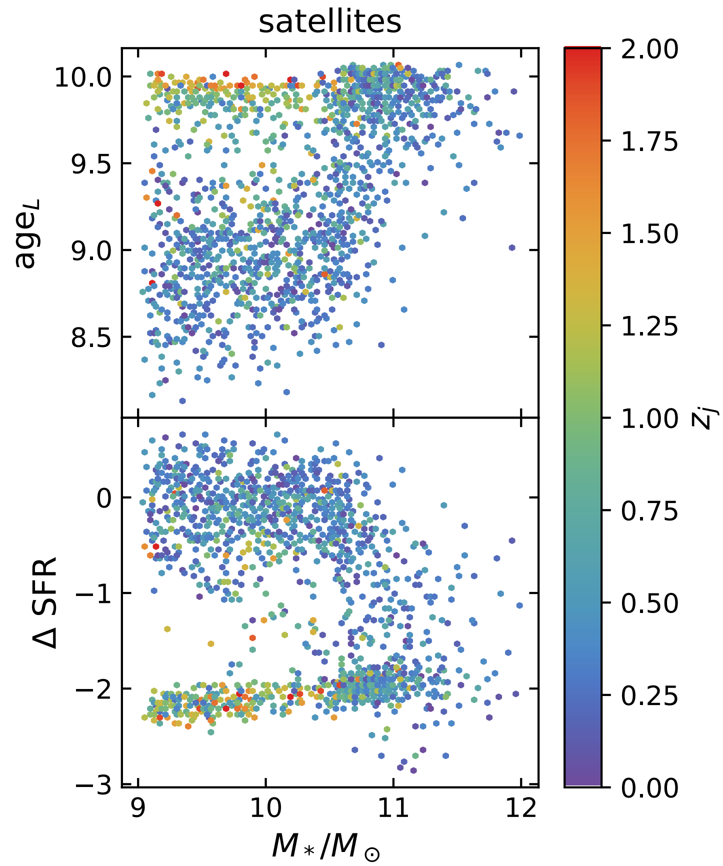

Figure 32. Formatting is identical to the right column of Figure 27, except points are colored by $z_{\rm j}$.

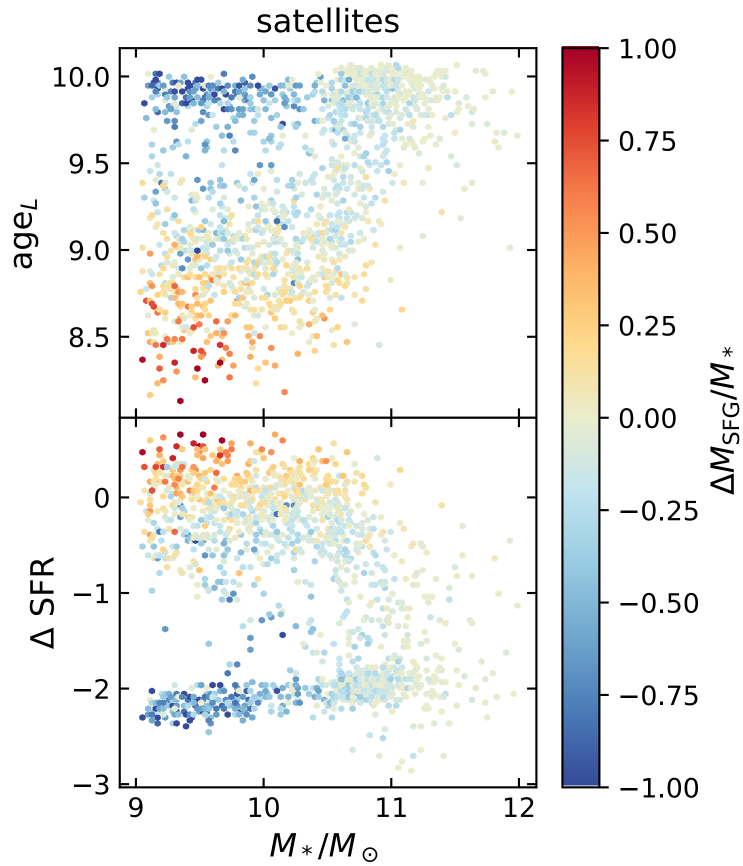

Figure 33. Formatting is identical to Figure 32, except points are colored by $\Delta M_{\rm SFG}$.